Monodisperse metal nanoparticle catalysts on silica mesoporous supports: synthesis, characterizations, and catalytic reactions

Gabor A. Somorjai* and Sang Hoon Joo

Department of Chemistry, University of California and Chemical Sciences and Materials Sciences Divisions, Lawrence Berkeley National Lab., Berkeley, California 94720

* To whom correspondence should be addressed (E-mail: somorjai@berkeley.edu)

Abstract

The design of high performance catalyst achieving near 100% product selectivity at maximum activity is one of the most important goals in the modern catalytic science research. To this end, the preparation of model catalysts whose catalytic performances can be predicted in a systematic and rational manner is of significant importance, which thereby allows understanding of the molecular ingredients affecting the catalytic performances. We have designed novel 3-dimensional (3D) high surface area model catalysts by the integration of colloidal metal nanoparticles and mesoporous silica supports. Monodisperse colloidal metal NPs with controllable size and shape were synthesized using dendrimers, polymers, or surfactants as the surface stabilizers. The size of Pt, and Rh nanoparticles can be varied from sub 1 nm to 15 nm, while the shape of Pt can be controlled to cube, cuboctahedron, and octahedron. The 3D model catalysts were generated by the incorporation of metal nanoparticles into the pores of mesoporous silica supports via two methods: capillary inclusion (CI) and nanoparticle encapsulation (NE). The former method relies on the sonication-induced inclusion of metal nanoparticles into the pores of mesoporous silica, whereas the latter is performed by the encapsulation of metal nanoparticles during the hydrothermal synthesis of mesoporous silica. The 3D model catalysts were comprehensively characterized by a variety of physical and chemical methods. These catalysts were found to show structure sensitivity in hydrocarbon conversion reactions. The Pt NPs supported on mesoporous SBA-15 silica (Pt/SBA-15) displayed significant particle size sensitivity in ethane hydrogenolysis over the size range of 1-7 nm. The Pt/SBA-15 catalysts also exhibited particle size dependent product selectivity in cyclohexene hydrogenation, crotonaldehyde hydrogenation, and pyrrole hydrogenation. The Rh loaded SBA-15 silica catalyst showed structure sensitivity in CO oxidation reaction. In addition,

Pt-mesoporous silica core-shell structured NPs (Pt@mSiO_2) were prepared, where the individual Pt NP is encapsulated by the mesoporous silica layer. The Pt@mSiO_2 catalysts showed promising catalytic activity in high temperature CO oxidation. The design of catalytic structures with tunable parameters by rational synthetic methods presents a major advance in the field of catalyst synthesis, which would lead to uncover the structure-function relationships in heterogeneous catalytic reactions.

1. Introduction

Recent drive towards green chemistry and environmentally-benign processes in industry ever-increasingly calls for a catalyst system that can achieve near 100% selectivity for only one desired product out of many possible products at maximum activity with long-term stability [1,2]. To achieve this goal, the understanding of molecular factors affecting catalytic performances is of immense importance, which would become possible by use of catalysts made by a designed or rational manner.

For the last few decades, the metal single crystals, by help of developments of surface science techniques and high-pressure reactor set-up, have been used to investigate elementary surface processes and mechanisms of surface reactions [3-5]. The single-crystalline metal surfaces inherently lack the structural complexity that are important elements in identifying the molecular factors for catalytic activity and selectivity, compared to the traditional industrial catalysts that consist of finely divided metal nanoparticles dispersed on the high surface area inorganic oxides. To bridge such a “materials gap”, the model catalytic systems have evolved from metal single crystals to lithographically-fabricated metal nanostructures on metal oxides, and to colloidally synthesized metal nanoparticles [6], as presented in Figure 1.

[Figure 1]

Industrially relevant heterogeneous catalysts are composed of active metal nanoparticles in the 1 - 10 nm size range which are supported on high surface area metal oxides or carbon. Of several methods for preparation of high surface area catalysts, the most prominent methods are ion-exchange and incipient wetness, in which the support material is impregnated with the metal precursors in solution, followed by thermal activation and/or H_2 reduction to form metal nanoparticles. Ion-exchange methods rely on an electrostatic interaction between metal precursor and oxide surface, and generally lead to high dispersion samples, whereas the incipient wetness methods that are achieved by physical forces (i.e. capillarity) are simple and easily implemented on a large scale. However, in both methods, the particle size is determined by the activation processes that are difficult to control, which generate in many cases the heterogeneity in particle size distribution.

We recently initiated a research program aimed at the rational design of 3-dimensional (3D) model catalysts with an ultimate goal of identifying molecular factors responsible for catalytic selectivity as well as activity and stability. Our strategy is the integration of two primary components of a supported catalyst; metal nanoparticles and oxide support, as outlined in Figure 2. The metal nanoparticles based on colloidal chemistry can be synthesized with controllable size and shape, while the mesoporous silicas with tailored pore size and pore connectivity are available. The hybridization of two catalytic entities would, therefore, enable the preparation of catalyst whose catalytic performances can be predicted in a defined and rational manner.

[Figure 2]

Our recent advances in 3D model catalysts using mesoporous silica supports are the main focus of this Chapter. The syntheses and characterization of size- and shape-controlled colloidal metal nanoparticles are explained, followed by a brief introduction to the mesoporous silica supports. The design, preparation, and physical and chemical characterization of 3D model catalysts constructed from metal nanoparticle and mesoporous supports are described. In final part, how parameters in 3D model catalysts such as particle size and shape would affect on the catalytic activity and selectivity are presented. Chosen catalytic reactions are highly relevant to the industrial process, include ethane hydrogenolysis, cyclohexene hydrogenation/dehydrogenation, crotonaldehyde hydrogenation, pyrrole hydrogenation, CO oxidation.

2. Synthesis and characterizations of 3-dimensional high surface area model catalysts prepared from monodisperse metal particles and mesoporous silica supports

2.1 Size- and shape-controlled metal nanoparticles fabricated by colloidal synthesis techniques

Recently, a considerable research effort has been devoted to the synthesis of metal nanoparticle based on the colloidal methods, which enabled them to be prepared with controlled particle size, shape, and composition [7-9]. In colloidal method for metal nanoparticle synthesis, in most cases, a metal salt precursor is reduced in solution in the presence of a stabilizing agent, which prevents an aggregation or improves the chemical stability of the generated nanoparticles. The colloidal nanoparticles prepared with optimized conditions are highly monodisperse with

size distribution below 10%.

We have been able to synthesize a variety of monometallic and bimetallic noble metal nanoparticles by alcohol or chemical reduction methods. We could prepare these nanoparticles with controlled particle size from 1 to 15 nm and shapes from cubes to cuboctahedra, and to octahedra as well as spheres. In this section, our recent progress toward the size and shape control of noble metal nanoparticles, mainly focused on the Pt and Rh, is described.

2.1.1 Size control of Pt & Rh nanoparticles of 1 – 15 nm

The size-controlled Pt and Rh nanoparticles could be prepared by the alcohol reduction methods. In alcohol reduction methods, alcohol serves both as a solvent for dissolving metal precursor and as a reducing agent for generating reduced metal colloids. Poly(vinylpyrrolidone) (PVP) was used as the surface stabilizing capping agent to prevent the aggregation of metal nanoparticles. The control of metal particle size could be achieved by regulating nucleation and/or growth kinetics, and the critical factors governing the kinetics were reduction temperature and concentration of metal precursors.

Pt nanoparticles with different particle sizes in the range of 1.7 – 7.1 nm were synthesized using dihydrogen hexachloroplatinate (H_2PtCl_6) as the Pt precursor in the presence of PVP [10,11]. Methanol, ethanol, and ethylene glycol (EG) were used as solvents for dissolving Pt salt and PVP, and as reducing agents for H_2PtCl_6. The 1.7 nm Pt particles were synthesized in the EG at 433 K. The Pt particle size increased to 2.6 and 2.9 nm upon lowering reaction temperature to 353 K in ethanol and 338 K in methanol, respectively. A continuous increase of the particle size with decreasing reaction temperature indicates that reduction of the Pt salts at lower temperature produces less amount of Pt nuclei in a short period, affording larger

size of Pt particles. The 3.6 nm Pt particles were successfully obtained by addition of 2.9 nm particles as seeds for stepwise growth. The 7.1 nm Pt particles were generated by slow and continuous alternating addition of the EG solution of Pt salt and PVP to boiling EG. The slow addition of Pt precursor ensured the maintenance of the nuclei concentration at a low level and continuously supplied Pt precursors were exclusively used-up for the overgrowth to the existing nuclei. The Pt particle sizes were measured by X-ray diffraction (XRD) and transmission electron microscopy (TEM). Average Pt particle sizes estimated by XRD were 1.7, 2.6, 2.9, 3.6, and 7.1 nm, and matched very well with TEM results. Figure 3 shows TEM images of Pt nanoparticles with varying particle sizes.

[Figure 3]

The synthesis of Rh nanoparticles was performed using rhodium acetylacetonate ($Rh(acac)_3$), as the precursor and butanediol as the solvent in the presence of the PVP stabilizer [12]. The size of the Rh nanoparticles could be controlled by changing the concentration of $Rh(acac)_3$ and reaction temperature. For instance, by gradually increasing the concentration of $Rh(acac)_3$ from 0.313 to 5 mM at the reaction temperature of 498 K, the Rh particle size increased from 5.4 to 10.4 nm. By lowering the reaction temperature to 478 K at $[Rh(acac)_3] = 5$ mM, the particle size further increased to 13.5 nm. It was observed that while heating the reaction mixtures to a designated temperature, the color change from orange-yellow to black occurred at a lower temperature for solutions containing higher concentrations of $Rh(acac)_3$. At the given temperature, therefore, a lower $Rh(acac)_3$ concentration gives rise to a slower reduction rate and decreased consumption of Rh ions during particle growth, resulting in a slower growth

rate of Rh nanoparticles. Consequently, under this condition, smaller monodisperse Rh nanocrystals are produced.

2.1.2 Dendrimer-templated synthesis of Pt and Rh nanoparticles

Metal nanoparticles whose size close to or less than 1 nm constitute an interesting class of materials. The nanoparticles of 1 nm have physicochemical properties that deviate from larger particles to a large degree. As compared to bulk metals, such nanoparticles exhibit shorter nearest neighbor distance, lower melting point, and higher ionization potential. It is therefore interesting to study whether 1 nm particles show catalytic activity different from that of bulk metal [13]. Catalytic metal nanoparticles as small as 1 nm were previously prepared on the zeolite supports by judiciously controlling the pretreatment conditions [14,15]. Recently, a dendrimer-templating method has been developed that enabled the preparation of 1 nm particles with various monometallic and bimetallic compositions [16-18]. The dendrimers are constructed with quasispherical hyperbranched polymers, and their structures and chemical properties can be controlled by changing core structure, the number and type of the duplicating units, and terminal functional groups. The most widely used dendrimers for metal nanoparticle preparations are polyamidoamine (PAMAM) and poly(propylene imine) (PPI).

We successfully synthesized Rh and Pt nanoparticles using PAMAM dendrimer as the template [19]. In the preparation of nanoparticles using the PAMAM dendrimer, metal ions are first complexed with tertiary amine groups of PAMAM, and upon the addition of $NaBH_4$ reductant metal nanoparticles are generated within the cavity of dendrimers (Figure 4). The size of prepared nanoparticles could be controlled at the ~ 1 nm range by varying the concentration of metal ions relative to the dendrimer. In this way, for example, Pt nanoparticles composed of 20

and 40 Pt atoms could be prepared, which corresponds to particle sizes of 0.8 and 1.0 nm, respectively. Figure 4 presents a typical TEM image of dendrimer-templated Pt nanoparticles, with each particle composed of 40 Pt atoms on a theoretical basis.

[Figure 4]

2.1.3 Shape control of Pt nanoparticles

The shape control of metal nanoparticles has recently been of intense interests. In particular, for catalytic applications, the nanoparticles with controlled shapes are intriguing as they represent the nanoscale mimics of extended metal single crystals, and therefore can be used as the model nanocatalysts. The shape control of noble metal nanoparticles can be realized by regulating the reduction kinetics of metal precursors and by manipulating the growth rates of the low index planes [7,8].

The addition of foreign ions (cationic or anionic) during the synthesis of metal nanoparticles was found to be an effective means for regulating the shapes of colloidal metals [20,21]. We employed a silver ion (Ag^+) as the shape-controlling agent during the synthesis of Pt nanoparticles, and could successfully control the shape of Pt nanoparticles (cube, cuboctahedra, and octahedra) [22]. The synthesis was performed using H_2PtCl_6 as the Pt precursor and PVP as the polymeric stabilizer in EG solution. The introduction of different amount of EG solution of $AgNO_3$ prior to the addition of Pt precursor induced morphology changes. The addition of 1.1 mol% Ag ion (with respect to the Pt concentration) afforded cubes with an 80 % yield. The increase in Ag^+ concentration to 11 and 32 mol% induced a gradual shape evolution to cuboctahedra and octahedra, respectively. All the particles with different shapes exhibited similar

particle sizes in the range of 9 - 10 nm (longest vertex-vertex distance) with narrow size distribution (~ 7%). The cubes expose (100) facets, and octahedra exhibit (111) facets exclusively. The intermediate cuboctahedra expose both (100) and (110) surfaces with the area ratio of 1 : 0.58. The shape evolution phenomenon by Ag ion indicates that the addition of Ag^+ enhances the (100) surface growth and/or suppresses the (111) direction growth. XRD and energy dispersive X-ray spectroscopy (EDX) indicated Ag was not present in these shape-controlled nanoparticles after removing excess Ag containing species (Ag^+ and AgCl) by repetitive washing-centrifugation. It was, however, later determined that residual Ag of up to 20 mol % of metal remained in the NPs. We found that Ag acts as a poison for the hydrogenation of ethylene by Pt, and the amount of Ag in the NPs can be directly correlated to the decrease in catalytic activity [23]. The remaining Ag species could be selectively removed by a wet etching method using HNO_3 (effective with concentration above 7 M) [24]. The shapes of the original particles were unchanged by an etching process, and the etched nanoparticles became highly active, as evidenced by an exponential increase of activity in ethylene hydrogenation after etching.

An alternative route to the shape control of Pt nanoparticle by chemical reduction method without the aid of foreign metal ions was developed [25]. The synthesis employed the K_2PtCl_4 as the precursor and tetradecyltrimethylammonium bromide ($C_{14}TABr$) as the stabilizer. In aqueous solution, the mixing of K_2PtCl_4 with $C_{14}TABr$ forms a liquid-crystalline phase. After heating at 323 K, the solution became clear pale yellow and then turned dark brown after reduction. Pt particle formation was observed over a broad range of reagent concentrations (20 – 200 mM $C_{14}TABr$ and 0.5 – 5 mM K_2PtCl_4) and ratios ($C_{14}TABr/K_2PtCl_4$ = 25 – 400). The

shapes of Pt nanoparticles could be controlled by varying the reduction method. When the sodium borohydride ($NaBH_4$) was used as the reducing agent, the shapes of nanoparticles evolved from dendritic structures to cuboctahedra (Figure 5a), and to cubes (Figure 5b) with a gradual increase in the amount of $NaBH_4$. On the other hand, porous particles of various sizes dominated when the reducing agent was ascorbic acid (Figure 5c). During the reaction of $NaBH_4$ with water, the pH value increases as a result of the formation of the strongly basic metaborate ion. Thus, the use of higher amount of $NaBH_4$ induces a higher pH, and this pH change is believed to induce the distinct morphology changes. The various control experiments conform to the conclusion that a higher pH value decreases the reduction rate, with slower reduction enabling selective growth on the (100) surfaces to produce cubic nanoparticles.

[Figure 5]

2.1.4 Simultaneous control of shape and size of Pt nanoparticles

The notion of structural dependence on catalytic activity and sensitivity significantly arises with nanoparticles less than 10 nm. The lack of a synthetic method for shaped nanoparticles in single-digit nanometer range reflects that size reduction while maintaining the shape is challenging. The difficulty is in part because the shape controlled nanoparticles are generally kinetically stable, but not thermodynamically stable. Therefore, change of any synthetic factor to reduce the size also causes shape to change. A new synthetic strategy to the simultaneous control of size and shape of Pt nanoparticles below 10 nm was developed [26]. Pt nanocubes and nanopolyhedra with tunable size from 5 to 9 nm were synthesized by controlling the reduction rate of metal precursors in a one-pot polyol synthesis. In this synthetic route, the

oxidation state of Pt precursor determined the nucleation step, thereby controlling the number of nuclei and the size of Pt particles, whereas the reaction temperature controlled the shape of Pt nanoparticles by regulation of the growth kinetics. The overall two-stage synthetic route to the size and shape control of Pt nanoparticle is schematically summarized in Figure 6.

[Figure 6]

For this synthesis, a mixture of ammonium hexachloroplatinate (IV) [$(NH_4)_2PtCl_6$, Pt(IV)] and ammonium tetrachloroplatinate (II) [$(NH_4)_2PtCl_4$, Pt(II)] and a teramethylammonium bromide ($N^+(CH_3)_4Br^-$) were used as the Pt precursor and the shape directing agent, respectively. In a typical synthesis, the metal salts [Pt(IV) and Pt(II)], the surfactants (PVP), and the shape directing agent (bromide ions) were dissolved in EG at room temperature to form a initial precursor solution. Previous studies have shown that the bromide species selectively adsorbed onto Pt (100) crystal faces and induce the formation of Pt nanocubes [25,27]. The mixed precursor solution was then rapidly heated to the desired temperature and maintained at the temperature for 20 min with vigorous stirring.

The formation of 9 (8.8 ± 1.2) nm (edge) Pt nanocubes (85% cubes, 15% tetrahedra or irregular crystals) is revealed by the TEM images (Figure 7a) when the Pt(IV) salt was used in the precursor solution. High resolution (HR) TEM image indicates that the Pt nanocubes are single-crystalline and enclosed by six (100) faces (inset of Figure 7a). During the synthesis, it was revealed that the 9 nm nanocubes were formed via a two-stage process. In the initial stage, the irregular Pt nuclei (ca. 3.5 nm) formed rapidly. In the second stage, the remaining Pt ions were reduced onto these nuclei with preferential growth direction along the [111] zone axis

because bromide ions stabilized the (100) faces. Based on this observation, smaller nanoparticles may form by either increasing the number of the nuclei in the initial stage or decreasing the remaining Pt ions in the second stage. The introduction of Pt(II) salt, which is reduced more easily and rapidly, to partially replace the Pt(IV) salt in the initial solution increased the number of nuclei in the first stage. By increasing the concentration ratio of Pt(II) to Pt(IV) in the initial solution, single-digit Pt nanocubes with sizes of 7 nm, 6 nm, and 5 nm were obtained (Figure 7b, c, and d, respectively) When all the Pt(IV) ions were replaced by Pt(II) ions in the initial solution, the 3.5 nm Pt nanocrystals were obtained (Figure 7f). We assumed that these 3.5 nm single-crystalline nanocrystals served as nuclei in single-digit nanocube synthesis. TEM images showed the monodispersity and well-defined shape of these Pt single-digit nanocubes and HRTEM images confirmed that these single-digit nanocubes are enclosed by six (100) faces. Figure 8 summarizes the size control of Pt nanocubes as a function of the ratios of Pt(IV) to total Pt ions. Pt nanocubes with sizes of 7 (6.9 ± 1.8) nm, 6 (5.9 ± 0.7) nm, and 5 (5.0 ± 0.4) nm were obtained when the ratios of Pt(IV) to total Pt ions (referred to as Pt(IV) ratio) was 0.8, 0.5, and 0.2, respectively.

[Figure 7]

[Figure 8]

The (100) faces of nanocubes are kinetically stabilized by bromide ions, therefore, the cubic shape of the single-digit nanoparticles was also kinetically tuned. By reducing the growth rate of the second stage via decreasing the temperature, the more thermodynamically stable polyhedral nanoparticles were obtained rather than cubic nanocrystals. For example, 5 nm single-

digit Pt spherical nanopolyhedra were synthesized when the Pt(IV) ratio was 20 and the temperature was 413 K (Figure 7e).

2.2 Mesoporous silica synthesis

For the last few decades, porous materials have been intensively studied with regard to technical applications as catalysts and catalyst supports [28]. The distribution of size, shape and volume of the void spaces in porous materials directly relates to their ability to perform the desired function in a particular application. From the viewpoint of materials, the porous material world had been governed by zeolites for several decades. The ion exchange capacity, tunable acid strength, and the well-defined pore diameters make zeolites very valuable for ion exchange, adsorption, separation and catalytic applications. However, pore size of zeolites (< 1.0 nm) inherently limited their applications with large molecules.

A new era of porous materials was opened up in 1992 following the discovery of a new family of silica based mesoporous molecular sieves designated as M41S by researchers at Mobil [29]. The mesoporous materials were synthesized using self-assembled supramolecular aggregates of amphiphillic molecules (surfactants or block copolymers) as the structure-directing agent [30,31]. The mesoporous silica materials have high surface area of ~ 1000 $m^2 g^{-1}$, and uniform, controllable mesopore diameter in the range of 2 - 50 nm, and these mesopores are periodically arranged. The discovery of mesoporous materials represents a breakthrough in the field of porous materials. Particularly for the catalytic application, the advent of mesoporous materials provided a new dimension in catalyst design beyond zeolite-dominated era, and their potential is currently under intense study in a variety of catalytic applications [32,33].

Since the synthesis of M41S family mesoporous materials by Mobil researchers, a

variety of mesoporous materials have been prepared via various synthetic pathways. Among these mesoporous materials, the SBA-15 (Santa Barbara Amorphous, number 15) and related mesoporous silicas, synthesized by using amphiphilic di- and tri-block copolymers as the templates, have larger uniform mesopores (up to 50 nm) and thicker walls (3 - 9 nm) than other mesoporous materials, making them ideally suited for catalytic applications [34]. In the present work, two types of mesoporous silicas, SBA-15 and MCF-17 (Mesocelluar Foam, 17) [35], have been used as the hosts for colloidal catalytic nanoparticles. The SBA-15 mesoporous silica is synthesized using triblock copolymer P123 ($EO_{20}PO_{70}EO_{20}$) as the structure-directing agent under acidic or neutral pH, and have pore size around 6 – 15 nm. The MCF-17, larger pore analogue of SBA-15, can be prepared in a similar way to the SBA-15, except the addition of pore-expanding agent such as trimethylbenzene to the reaction mixture. The pore size of MCF mesoporous silica ranges from 20 – 50 nm. The synthesis details of these silicas have been described elsewhere [34,35].

2.3 Metal nanoparticles dispersed in mesoporous silica supports by capillary inclusion and encapsulation methods

The high surface area 3D model catalysts were generated by combining two distinct structural components (colloidal nanoparticles and mesoporous silica supports). The colloidal metal nanoparticles were incorporated into the pores of mesoporous silica supports by two methods: capillarity-induced physical inclusion [36] and in situ encapsulation during the hydrothermal growth of mesoporous silica [37].

2.3.1 Capillary inclusion method

The capillary inclusion (CI) method is based on the sonication-induced inclusion of metal nanoparticles into the pores of mesoporous silica [36]. A series of Pt nanoparticles with different sizes (1.7 – 7.1 nm) were prepared by alcohol reduction methods. SBA-15 mesoporous silica with an average pore diameter of 9.0 nm that is large enough to incorporate Pt nanoparticles was used as the support. Prior to inclusion of PVP-protected Pt nanoparticles, the SBA-15 silica is calcined at 823 K for 12 hours to remove residual templating polymer. Pt nanoparticles were mixed with SBA-15 in a 1:1 v/v mixture of water and ethanol. Low power sonication for 3 h at room temperature led to the homogeneous dispersion of Pt nanoparticles throughout the entire channel structures of SBA-15 without disruption of uniform channel structures. It was found that, without sonication, Pt nanoparticles adsorbed primarily on the external surface of SBA-15 and its mesopore openings. Sonication promotes homogeneous inclusion and deposition of Pt nanoparticles on the inner surface of the SBA-15 mesopores. Different size metal nanoparticles were successfully incorporated into the mesoporous SBA-15 yielding Pt(X)/SBA-15 catalysts (X = 1.7, 2.6, 2.9, 3.6, and 7.1 nm).

For the incorporated Pt nanoparticles to be catalytically active, the PVP stabilizer should be effectively removed. The calcinations of Pt/SBA-15 catalysts were performed in pure oxygen for 12 – 24 h at temperatures ranging from 623 – 723 K. Catalysts were activated in He for 1 h and reduced at 723 K in H_2 for 1 hour. After removal of PVP, the particle size was determined by chemisorption. Table 1 is a summary of chemisorption data and particle sizes deduced by chemisorption and XRD for CI catalysts. Fractional dispersions for the Pt/SBA-15 catalysts ranged from 0.13 to 0.31 based on total H_2-O_2 titration uptakes [38] for supported Pt nanoparticles ranging from 1.7 to 7.1 nm. A 3.2% Pt/SiO_2 catalyst prepared by ion exchange (Pt/SiO_2-IE) [39] used as a standard had an irreversible measured uptake corresponding to a

dispersion greater than unity. The Pt particle size based on chemisorption was calculated according to the equation d (nm) = 1.13/D, where D is the metallic dispersion [40]. Particle size calculated from chemisorption trends with TEM and XRD particle size of the free-standing particles. However, as shown in Table 1, there is a significant difference in the measured particle size between chemisorption and XRD, as the values deduced from chemisorption were lower than those determined by XRD. Synthesis of the Pt nanoparticles requires the use of a capping polymer that prevents particles from agglomerating while in solution. It is suggested that PVP bonds strongly to the Pt surface and difficult to remove when the particles are dispersed within the SBA-15 matrix, even after careful calcinations. The discrepancy between chemisorption and XRD particle size is due to the reduction of exposed surface area because of remaining polymer on the Pt surface. XRD would be insensitive to this circumstance, while chemisorption would directly probe this loss of surface area.

2.3.2 Nanoparticle encapsulation method

Although the mechanical incorporation of nanoparticles is very effective for the general synthesis of 3D catalysts, the size of particles that can be incorporated into the mesopores are inherently limited by the pore diameters of mesoporous silica supports. To circumvent this limitation, an alternative approach referred to as nanoparticle encapsulation (NE) was developed [37]. In the 3D catalyst design by NE method, Pt nanoparticles were incorporated within the silica matrix during the hydrothermal growth of mesoporous silica structures.

For the effective dispersion of metal particles the synthesis of SBA-15 was performed under neutral condition, as the acidic conditions of general SBA-15 synthesis [34] cause precipitation of metal nanoparticles without silica encapsulation, or the formation of amorphous

silica due to the presence of surfactants used for the nanoparticle synthesis. Pt nanoparticles with different sizes were dispersed in the aqueous template block copolymer (P123) solution, and sodium fluoride (silica polymerization catalyst) and tetramethyl orthosilicate (TMOS, silica source) were added to the reaction mixture [41]. The slurry was aged at 313 K for a day, followed by an additional day at 373 K. The precipitates were extensively washed with ethanol, followed by drying at 373 K. Pt/SBA-15 catalysts were then calcined at temperatures ranging from 623 – 723 K. It appears that Pt nanoparticles remain highly dispersed in the reaction mixture during mesostructure formation, and no severe aggregation of nanoparticles occurred during calcinations, as revealed by TEM images of Pt/SBA-15 catalysts after calcinations (Figure 9). All characterizations including XRD, small angle XRD, nitrogen physisorption, and TEM indicated a formation of well-ordered mesoporous silica structure (Figure 9 and 10). Pt/SBA-15 catalysts have uniform mesopores (11.2 – 11.3 nm) and high surface areas (523 – 661 $m^2 g^{-1}$). The Pt content in final catalysts determined by elemental analysis was 0.6 – 0.77% with respect to the total catalyst weight.

[Figure 9]

[Figure 10]

Selective gas adsorption experiments on the catalyst surface were performed, and the results are listed in Table 1. Particle sizes calculated based on H_2-O_2 titration measurements over NE-series Pt/SBA-15 catalysts are in better agreement with TEM and XRD calculated sizes of the free-standing particles, compared to catalysts prepared by CI method (see section 2.3.1). The better agreement is most likely due to a more complete removal of PVP. After the hydrothermal

synthesis, the NE catalysts are washed with copious amounts of water and ethanol to remove the triblock copolymer used to template the silica mesostructure. PVP is soluble in both solvents and PVP may be removed from the particle surface during washing, followed by the thermal calcination. Infrared spectroscopic investigation of CO adsorption on the NE catalyst series confirmed that combination of washing and calcination was sufficient for PVP removal (although C-H and C=O bands due to PVP were observed), and further confirmed the monodisperse nature of the nanoparticle catalysts. Figure 11 displays the infrared spectra of atop bound CO on the NE series of reduced catalysts [37]. The peak position blue-shifts by more than 15 cm^{-1} as the particle size increases from 1.7 to 7.1 nm, while the peak width decreases as the particle size increases suggesting that the number of energetically distinct sites capable of adsorbing CO decrease with increasing particle size. These observations are in agreement with statistical calculations of the fraction of different surfaces atoms for idealized shapes [42]. As the particle size increases, a majority of the surfaces atoms are found in large terraces, in which all atoms have essentially the same reactivity, but in the case of smaller particles, the fraction of surface atoms at edge or corners becomes significant, and their influence is felt by incoming adsorbates and their adsorbed counterparts. NE catalysts were additionally characterized by ethylene hydrogenation. The intrinsic activity measured on a per gram Pt basis was higher than that of the corresponding particle size in the CI series catalysts, and TOFs were a factor five higher on the NE series (~ 3.5 s^{-1}), as listed in Table 1. Overall, the results from chemisorption, IR spectroscopy using CO probe, and reactivity for ethylene hydrogenation demonstrate that the catalyst surface of Pt/SBA-15 catalysts prepared by NE method is mostly free of PVP.

[Figure 11]

[Table 1]

The NE method for model 3D catalysts was later extended to the preparation of Rh/SBA-15 catalysts from size-controlled Rh nanoparticles (1.9 – 11.3 nm), demonstrating the effectiveness of the method [43]. Figure 12 presents TEM images of Rh/SBA-15 catalysts with different Rh sizes.

[Figure 12]

2.4 Metal-mesoporous silica core-shell nanoparticles

Model catalytic systems based on colloidal nanoparticles have shown that the thermal and chemical stabilities of nanoparticle catalysts as well as catalytic activity and selectivity are of prime importance [44]. Colloidal nanoparticles that are usually prepared in the presence of organic capping agents are subject to the deformation and aggregation under high temperature treatment, typically above 573 K. Hence, the size, shape, and composition of the nanoparticles during or after high-temperature reactions could be different from those of pristine nanoparticles. Many industrially important catalytic processes are carried out at temperatures above 573 K [45-47]. The model catalysts that are stable at high reaction temperatures are, therefore, in high demand. A core-shell Pt/mesoporous silica (Pt@mSiO_2) structure was designed for thermally stable catalytic systems [48]. In the core-shell particle structures, the outer shells isolate the catalytically active nanoparticle cores and prevent the possibility of sintering of core particles during catalytic reactions at high temperatures. In addition, the synergistic effects of metal-support interfaces may be maximized where such interfaces are important in catalytic

performances.

The strategy for Pt@mSiO_2 structures is outlined in Figure 13. First, Pt nanocubes were synthesized using developed procedure in our group that employed TTAB as the capping and structure directing agent. Then, a mesoporous silica shell was grown from tetraethylorthosilicate (TEOS) around the capped Pt nanocubes (Figure 14a). After calcination to remove TTAB, the silica shell became porous. The Pt@mSiO_2 consisted of 14 nm Pt cores and 17-nm-thick mesoporous silica shells (Figure 14b).

[Figure 13]

[Figure 14]

Nitrogen physisorption experiments revealed that the Pt@mSiO_2 particles were mesoporous, and pore size and Brunauer-Emmett-Teller surface area of Pt@mSiO_2 were 2.3 nm and 440 m^2 g^{-1}, respectively. For core-shell nanoparticles to be catalytically active, direct access of reactive molecules to the core particles is crucial. The accessibility of gas molecules was directly proved by chemisorption measurements. Hydrogen chemisorption over the Pt@mSiO_2 catalyst gave a dispersion value of 8 ± 0.5%, which is comparable to the ratio of surface atoms (11%) on the Pt particle, as calculated by geometric considerations. The activity of Pt cores in the core-shell Pt@mSiO_2 nanoparticles was further explored ethylene hydrogenation. The ethylene hydrogenation was carried out at 10 Torr of ethylene, 100 Torr of H_2, with the balance He. The Pt@mSiO_2 exhibited a turnover frequency (TOF) of 6.9 s^{-1} at 298 K and an activation energy of 8.1 kcal mol^{-1}. The TOF and activation energy are similar to those of the Pt single crystal [49], colloidal-Pt-nanoparticle-loaded SBA-15 model catalysts [36,37], and other supported catalysts

[50,51]. All the evidences conform to the fact that the catalytically active Pt core in Pt@$mSiO_2$ nanoparticles are directly exposed to the reacting molecules through the mesopores within the silica shells.

The thermal stability of Pt@$mSiO_2$ core-shell particles was investigated. After calcination at 623 K, the spherical core-shell shape of the as-synthesized Pt@$mSiO_2$ NPs was maintained. The shape of Pt cores inside Pt@$mSiO_2$ became slightly rounder after the calcination than that of Pt in as-synthesized Pt@$mSiO_2$, which is presumably due to the melting of the Pt particles at the interface of Pt-silica. After the calcination at 823 K, the core-shell morphology of Pt@$mSiO_2$ nanoparticles was preserved (Figure 14c). Even upon heating the sample as high as 1023 K, the morphology of most Pt@$mSiO_2$ nanoparticles was maintained and the Pt cores were encaged within the silica shells (Figure 14d), indicating high thermal stability of Pt@$mSiO_2$ core-shell nanoparticles.

3. Catalytic properties of 3-dimensional model oxide supported metal nanoparticle catalysts

3.1 Ethane hydrogenolysis by Pt/SBA-15

The hydrogenolysis of alkanes has been studied extensively because of the well-known sensitivity of hydrogenolysis rates on surface structure [52,53]. As a test of particle surface structure, the hydrogenolysis of ethane was examined over the Pt/SBA-15 catalysts prepared by nanoparticle encapsulation method [36]. Highly dispersed, ion-exchanged silica supported Pt catalyst (3.2% Pt/SiO_2-IE) was also tested for comparison. Ethane hydrogenolysis was performed with 20 Torr C_2H_6, 200 Torr H_2 in a temperature range from 593 – 673 K. The kinetic data for ethane hydrogenolysis are summarized in Table 2 and the influence of particle size on

catalytic activity and the measured apparent activation energy are shown in Figure 15. Ethane hydrogenolysis is sensitive to particle size with turnover frequencies varying by at least two orders of magnitude for catalysts containing Pt particles from 1 – 7 nm with ion-exchanged 3.2% Pt/SiO_2-IE (particles of ~ 1 nm) the most active (6.4×10^{-2} s^{-1} at 658 K). The 3.2% Pt/SiO_2-IE catalyst had an apparent activation energy of 54 kcal mol^{-1}, and apparent activation energy linearly increased up to ~ 75 kcal mol^{-1} on the 0.6% Pt(3.6 nm)/SBA-15 catalyst, after which the activation energy is unchanged with larger particle size. Apparent reaction orders in ethane and hydrogen were 1 and ~ -3, respectively. The observed reaction orders are in agreement with measurements on other supported Pt catalysts [54].

[Table 2]

[Figure 15]

Large ensembles of Pt atoms are necessary for ethane hydrogenolysis because the C_2 intermediate is most likely bonded to multiple Pt atoms and adjacent sites are needed for H adsorption. Besides an existence of large ensemble, the proper spatial orientation of the metal atoms was also suggested as the requirement for an active site for ethane hydrogenolysis [55,56]. The number of atoms in the ensemble varies with metal presumably due to the stoichiometry of the C_2H_x species in which the C-C bond is broken. In the case of Pt, the proposed C_2 intermediate that undergoes C-C bond cleavage is the ethyl radical, C_2H_5 [57,58]. In this case, the ensemble size may be significantly reduced but the orientation of the atoms composing the ensemble is still critical; most likely requiring a fraction of the ensemble to be composed of atomic steps, kinks, or other sources of surface roughness. Theoretical calculations of C_2H_x species fragment stability

on Pt slabs and clusters have shown that barriers to bond activation are lower on a stepped Pt(211) surface relative to a flat (111) surface [59,60]. Correspondingly, the activated complexes along the hydrogenolysis reaction coordinate are stabilized on the stepped surface relative to the flat surface. Small metal crystallites have a higher proportion of coordinatively unsaturated surface atoms, analogous to a stepped single crystal, while the surfaces of large Pt particle are terminated primarily by low index, high coordination surfaces. It appears that reactions involving CH and their activated complexes occur on these defect sites because they provide more stable bonding. The identity of the active site for C-H and C-C bond activation is unknown, but particle size dependent catalytic behavior of ethane hydrogenolysis suggests that surface roughness is a primary component of the active site.

3.2 Cyclohexene hydrogenation/dehydrogenation by Pt/SBA-15

The influence of particle size on selectivity is in general difficult to study because it is often subtle, therefore requiring materials with very controlled and defined properties. The monodisperse 1.7 - 7.1 nm Pt particles we have synthesized are, therefore, excellent candidates for selectivity studies. The hydrogenation-dehydrogenation of cyclohexene was chosen as a model reaction for particle size-dependent selectivity study [61]. The cyclohexene conversion was examined over the same set of Pt catalysts used for ethane hydrogenolysis (see section 3.1). The reactions were performed H_2-excess conditions with 10 Torr C_6H_{10} and 200 – 600 Torr H_2 in the range of 273 – 650 K. The change of TOF and activation energies for both hydrogenation and dehydrogenation of cyclohexene by Pt/SBA-15 catalysts are listed in Table 3.

[Table 3]

The conversion of cyclohexene in the presence of excess H_2 (H_2: C_6H_{10} ratio = 20 – 60) was characterized by three regimes: hydrogenation of cyclohexene to cyclohexane at low temperature (< 423 K), an intermediate temperature range in which both hydrogenation and dehydrogenation occur; and a high temperature regime in which the dehydrogenation of cyclohexene dominates (> 573 K). The rates of both reactions demonstrated maxima with temperature, regardless of Pt particle size. For the hydrogenation of cyclohexene, a non-Arrhenius temperature dependence (apparent negative activation energy) was observed. Hydrogenation to cyclohexane is structure insensitive at low temperatures, and apparently structure sensitive in the non-Arrhenius regime; the origin of the particle-size dependent reactivity with temperature is attributed to a change in the coverage of reactive hydrogen [60]. On the other hand, dehydrogenation reaction to benzene exhibited sensitivity to the particle size, as smaller particles were more active and had lower apparent activation energies than larger particles.

A distinct selectivity exerted by Pt particle size was demonstrated at the intermediate temperature (423 K) with 10 Torr C_6H_{10}, 200 Torr H_2, as shown in Figure 16. The selectivity to benzene was highest (> 60%) on the 1 nm particles (3.2% Pt/SiO_2-IE) and subsequently decreased to less than 10% on large (7.1 nm) particles. Upon raising the reaction temperature to 523 K (Figure 16 inset), the selectivity to benzene is > 60% for all particle sizes, although the selectivity to cyclohexane increases with particle size. This demonstrates that the ability of a particle to change the major product is applicable only under certain experimental conditions.

[Figure 16]

The selectivity to hydrogenation–dehydrogenation products during cyclohexene conversion over a wide temperature range is also facet-dependent, as demonstrated by Somorjai and co-workers [63-65]. On Pt(100) at 423 K, the selectivity to cyclohexane (10 Torr C_6H_{10}, 100 Torr H_2) is 82%, while the corresponding selectivity is 75% on Pt(111). At 523 K, the higher selectivity to the hydrogenation product is now measured on the (111) surface (~34%), while the hydrogenation selectivity on Pt(100) is only ~14% (see Figure 16 inset). Figure 16 demonstrates that the selectivity for both single crystals matches that of the 3 nm diameter particle, while the selectivity at 523 K indicates the (111) single crystal behaves more like the largest Pt particle, and the Pt(100) continues to behave like the Pt(2.9 nm)/SBA-15 catalyst. The NPs used in this study do not demonstrate well-defined changes in shape with particle size; therefore, we believe that the influence of particle size on reaction selectivity is related to changes in the average coordination number of the atoms within the NPs rather than the shape of the nanoparticle.

3.3 Crotonaldehyde hydrogenation by Pt/SBA-15

The hydrogenation of crotonaldehyde is of fundamental scientific interest because two different types of unsaturated chemical bonds (C=C and C=O) are present in the same molecule, serving as a useful probe of heterogeneous catalytic selectivity [67]. Accordingly, this multipath reaction was selected as a model reaction for investigating Pt size effect on the catalytic selectivity [65].

The crotonaldehyde hydrogenation was performed with 8 Torr crotonaldehyde, 160 Torr H_2 in the temperature range of 353 – 393 K over Pt/SBA-15 catalysts used for ethane hydrogenolysis and cyclohexene hydrogenation/dehydrogenation. Butyraldehyde was obtained

as the major product of crotonaldehyde hydrogenation over all catalysts and the entire temperature range (353–393 K), which forms by the selective hydrogenation of the C=C bond. The minor products are crotyl alcohol (the second most abundant product) formed by selective hydrogenation of the C=O bond, butanol (complete hydrogenation of C=C and C=O), and propylene and propane (decarbonylation) (Scheme 1). The temperature dependence for hydrogenation was similar for all catalysts studied. The overall apparent activation energy for the consumption of crotonaldehyde was independent of the particle size (Table 4). The apparent activation energy for the individual products is also independent of particle size: 16–17 kcal mol^{-1} for C=C hydrogenation to butyraldehyde, 7–10 kcal mol^{-1} for C=O hydrogenation to crotyl alcohol, 10–15 kcal mol^{-1} for the complete hydrogenation to butanol, and 11–12 kcal mol^{-1} for decarbonylation. The reaction order in H_2 (not shown) was unity at 353 K. These observations are consistent with general trends of crotonaldehyde hydrogenation over Pt catalysts that have been reported previously [67].

[Scheme 1]

[Table 4]

The steady-state TOF and reaction selectivity to crotyl alcohol at 353 K for all catalysts are shown in Table 4 and Figure 17. The overall rate and selectivity to crotyl alcohol increased monotonically with increasing particle size. With an increase in the particle size from 1.7 to 7.1 nm, the steady-state rate increased by a factor of ~ 2 (from 2.1×10^{-2} to 4.8×10^{-2} s^{-1}) and the selectivity towards crotyl alcohol varied by a factor of ~ 3 (from 13.7 % to 33.9 %).

[Figure 17]

The tendency of high selectivity toward crotyl alcohol with increasing particle size has been well-documented in previous literatures [67,69-71], and the role of particle size may be explained in a combination of three factors. The first is related to the fraction of exposed atoms in close packed (111) planes versus those at coordinatively unsaturated sites or in open faces such as (100) or (110). Crotonaldehyde preferentially adsorbs via a di-σ bond of C=O on the (111) surface of Pt, while on the (100) surface, it bonds to the surface in a flat geometry (η^4 configuration) through both of its π-bonds [14]. On the (110) surface, the most corrugated of the three lowest energy fcc surfaces, crotonaldehyde bonds via its C=C π-bond [72]. The increase in selective C=O interaction on (111) facets is responsible for the increased selectivity towards the unsaturated alcohol. Larger nanoparticles have a larger fraction of atoms in terraces with a close packed structure than smaller particles and are selective for the formation of crotyl alcohol [71]. The second reason for particle size dependent selectivity is the steric hindrance of the C=C bond, which is more easily accommodated on smaller nanoparticles. Catalytic activity is also lower over smaller nanoparticles because decarbonylation of crotonaldehyde to CO and C3 hydrocarbons as well as other C–C bond breaking reactions occur preferentially on the corner and edge sites that are more prevalent on smaller particles: CO and carbon deposits from C–C bond breaking poison the catalyst surface.

3.4 Pyrrole hydrogenation by Pt/SBA-15

The new fuel quality regulations increasingly require a high level of hydrodenitogenation (HDN) to achieve a desirable conversion of other hydroprocessing reactions

[73]. The understanding of HDN process through model reaction studies is therefore of significant importance. An aspect of HDN chemistry was investigated with size- and shape-controlled Pt nanoparticles using pyrrole hydrogenation as a model reaction [74]. Pyrrole was selected as the reactant because organics with five-membered N-containing rings are the most common components in fuel [75,76].

The size-controlled Pt particles between 0.8 to 5 nm were synthesized by two synthetic methods. The 0.8, 1.0, and 2.0 nm Pt nanoparticles were prepared by dendrimer-templating approach using the fourth generation hydroxyl terminated polyamidoamine (PAMAM) dendrimers as the templating and capping agent. The larger Pt particles (1.5, 2.9, and 5.0 nm) were obtained by the alcohol reduction methods. The Pt nanoparticles were then loaded into the pores of SBA-15 mesoporous silica by capillary inclusion method. Pyrrole hydrogenation activity over Pt/SBA-15 catalysts was measured at 413 K in 4 Torr pyrrole and 400 Torr H_2 with a He balance. The steady-state TOFs for hydrogenation of pyrrole (Scheme 2) were compared at equal pyrrole conversions (11 ± 2%), which is necessary for selectivity comparisons. TOFs for pyrrolidine formation were found to be ~ 70 ks^{-1} except for the smallest Pt size, proving the structure insensitivity of formation of C-H bonds [77,78]. For *n*-butylamine formation, TOFs increased as the Pt particle size increased. This structure sensitivity for the ring opening led to differences in product selectivity (Figure 18). Particularly for nanoparticles smaller than 2 nm, selectivity was a strong function of size as pyrrolidine formation occurred more easily over smaller sizes. As Pt particle size increased above 2 nm, behavior became independent of size with *n*-butylamine selectivity approaching 100%.

[Scheme 2]

[Figure 18]

The reaction results demonstrated that the ring opening was more facile over larger Pt nanoparticles, leading to almost entirely *n*-butylamine, compared to smaller ones, which formed both pyrrolidine and *n*-butylamine. The selectivity in pyrrolidine hydrogenation is presumably due to the *n*-butylamine product poisoning. The N of *n*-butylamine is more electron-rich than its counterparts in pyrrole and pyrrolidine, and thus can form stronger bonds with the surface and consequently inhibit turnover. As the particle size decreases, the portion of coordinatively unsaturated sites such as steps and kinks over flat terrace sites dramatically increases. Thus, electron-rich *n*-butylamine can more strongly interact with the surfaces of smaller Pt nanoparticles. In addition, the metallic character of Pt nanoparticles decreases with diminishing particle size, possibly inducing the stronger interaction of *n*-butylamine. The product poisoning by *n*-butylamine may be explained by either structural or electronic effect.

The Pt nanoparticle shape effect on the selectivity of pyrrole hydrogenation was also examined using 5 and 9 nm Pt nanocubes and 5 nm nanopolyhedra [26]. Pyrrole hydrogenation of these nanoparticle was examined after they were incorporated into MCF mesoporous silica by capillarity inclusion method. As shown in Figure 19, the shape of the single-digit nanocrystals led to product selectivity differences. For both 5 nm and 9 nm Pt nanocubes, *n*-butylamine was the dominant product at all studied temperatures. For the 5 nm spherical nanopolyhedra, however, pyrrolidine (up to 30%) and *n*-butylamine were both formed at lower temperatures. The structure sensitivity exerted by Pt particle shape was substantiated with the sun frequency generation (SFG) vibrational spectroscopy study. The SFG spectra of Pt (111) and Pt (100) single crystals recorded during pyrrole hydrogenation at 298 K showed that the CH_2 group bands contributed by

disorder in the butyl chains of *n*-butylamine and the CH_3 group bands on Pt (100) single crystal were relatively stronger than the ones on Pt (111) single crystal. The result suggested that the amount of *n*-butylamine on the Pt surface was greatly enhanced on the (100) crystal surface. Based on this observation, the shape-controlled selectivity of pyrrole hydrogenation should be caused by the hydrogenation of pyrrolidine to *n*-butylamine being promoted by the Pt (100) surface. Since the Pt nanocubes are mainly enclosed by (100) surfaces, pyrrolidine was converted into *n*-butylamine on the surface of the nanocubes. Therefore, nanocubes promote the formation of *n*-butylamine at lower temperatures. By contrast, the nanopolyhedra exposing more thermodynamically stable (111) surfaces inhibit the turnover of *n*-butylamine.

[Figure 19]

3.5 CO oxidation by Rh/SBA-15

The catalytic oxidation of CO to CO_2 has been one of the most widely studied surface reactions owing to its significance for emission control and fuel cells [79-82]. Although many investigations of CO oxidation over Rh catalysts have been carried out, the dependence of the CO oxidation rate on the Rh particle size is not clearly understood yet. To address this issue, particle size dependence for CO oxidation over SBA-15 silica supported Rh nanoparticles of 1.9 – 11.3 nm was investigated [43].

A series of PVP stabilized Rh nanoparticles with sizes of 1.9, 2.4, 3.6, 5.1, 6.7, and 11.3 nm were prepared and they were supported onto mesoporous silica SBA-15 by nanoparticle encapsulation. The resulting Rh/SBA-15 catalysts were studied in either as-synthesized form with no pretreatment or after a pretreatment of high temperature O_2 calcination and subsequent

H_2 reduction. CO oxidation by O_2 at 40 Torr CO and 100 Torr O_2 was investigated as a function of Rh particle size over as-synthesized and pretreated Rh/SBA-15 catalysts. From the TOF at 413 K shown graphically in Figure 20, a few clear trends emerge. The as-syntheized samples are more active than the calcined ones. For the as-synthesized catalysts, TOF at 170 °C increased from 0.4 to 1.7 s^{-1} with decreasing particle size from 11.3 to 1.9 nm, whereas for the catalyst series after calcination and reduction, the TOF was between 0.1 and 0.4 s^{-1} with no clear particle size dependence. The particle size dependence observed for as-synthesized catalysts is similar to the trend observed in our previous study of similar Rh nanoparticles, which were deposited onto silicon wafers by Langmuir-Blodgett (LB) deposition [83]. In our work with LB films of these particles we observed that smaller particles are more facilely oxidized during CO oxidation by ambient pressure X-ray photoelectron spectroscopy and attributed the observed size-dependent TOF to this phenomenon.

[Figure 20]

To access the change in particle size dependency observed for samples before and after high temperature pretreatments, the adsorption of CO on the Rh nanoparticle surfaces before calcination, after calcination, and after calcination followed by *in situ* reduction was examined using *in situ* diffuse reflectance infrared Fourier-Transform spectroscopy (DRIFTS). The DRIFTS study revealed that the mode of CO adsorption was influenced by the heat treatments. CO adsorbs at two distinct bridge sites on as-synthesized Rh/SBA-15, attributable to metallic Rh(0) and oxidized Rh(I) bridge sites. After calcination in O_2, CO adsorbs solely to atop Rh sites, with both Rh(0) and Rh(I) available. Following *in situ* reduction by H_2, all Rh is converted to

Rh(0) and only atop CO on Rh(0) is observed. Figure 21 summarizes treatment-dependent change of CO adsorption mode of Rh/SBA-15 catalysts.

[Figure 21]

In correlating the activity trend and CO adsorption mode, the bridge-bound CO reacts with oxygen in a structure sensitive manner (as-synthesized samples), while the reaction between atop CO on Rh(0) sites and surface oxygen is structure insensitive (heat treated samples). Additionally, the as-synthesized samples, on which CO adsorbs at bridge sites, exhibit higher catalytic activity. The high activity endowed by the CO adsorbed on bridge sites in as-synthesized Rh/SBA-15 catalysts may be influenced by the presence of intact PVP stabilizer. In as-synthesized samples, the carbonyl in the pyrrolidone ring of PVP may interact with Rh atoms, stabilizing higher oxidation states of Rh and changing the predominant mode of CO adsorption from atop to bridge sites. The reaction between O_2 and atop CO is independent of particle size and the reaction rate for Rh NP catalysts is similar to that over Rh single crystals [84]. The reaction rate of bridge CO with O_2, however, is particle size dependent. Thus, PVP “imposes” a particle size dependent rate on the Rh nanoparticles by altering the adsorption behavior of CO to favor bridge sites over atop sites.

The induced structure sensitivity may arise from two different sources. In our previous work, we demonstrated that the smaller PVP capped Rh NPs are more oxidized during CO oxidation than the larger particles. This increased oxidation may give rise to a larger percentage of more active surfaces. A second possible explanation arises from the infrared spectroscopy. CO adsorbed at bridge sites may be more influenced by the particle size than atop CO, which

involves a single surface Rh atom.

3.6 CO oxidation by Pt-mesoporous silica core-shell nanoparticles

The core-shell structured Pt@mSiO_2 nanoparticles were prepared with an aim of designing thermally stable nanocatalysts. High-temperature catalytic properties of Pt@mSiO_2 core-shell nanoparticles were explored by using CO oxidation as a model reaction. For the CO oxidation reaction, the Pt@mSiO_2 and Pt nanoparticles were deposited on a silicon wafer using the LB technique. CO oxidation was carried out with excess O_2 (40 Torr CO, 100 Torr O_2, with the balance He) in the temperature range of 513 – 613 K. Figure 22 shows the CO oxidation activity of the Pt@mSiO_2. Two distinct reaction regimes are observed as a function of temperature, which indicated an ignition temperature around 563 – 573 K. For comparison, the TTAB-capped Pt nanoparticle catalyst on the silicon wafer was also tested for CO oxidation. The activity of the Pt@mSiO_2 catalyst was as high as that of TTAB-capped Pt nanoparticles, indicating that the silica shells in the Pt@mSiO_2 nanoparticles were porous enough to provide access to the Pt cores, which is consistent with chemisorption and ethylene hydrogenation studies. Figure 23 comparatively shows scanning electron microscope (SEM) and TEM images of TTAB-capped Pt nanoparticle arrays on the silicon wafer and Pt dispersed inside the mesopores of mesostructured cellular foam (MCF) silica (Pt/MCF-17), as well as the core-shell Pt@mSiO_2 before and after CO oxidation. The Pt@mSiO_2 catalyst after CO oxidation at 603 K maintained the morphology of calcined particles (Fig. 23d). However, the TTAB-capped Pt on silicon wafer (Fig. 23e) and Pt/MCF-17 (Fig. 23f) exhibited severe aggregation of Pt particles after CO oxidation at 573 K, which hampered the quantitative study of CO oxidation above the ignition temperature regime.

[Figure 22]

[Figure 23]

The ignition temperature during CO oxidation over the Pt@mSiO$_2$ catalyst was found to be 563 – 573 K, which lies between that of Pt(100) (500 K) and Pt(111) (620 K) single crystals [85]. The Pt cores encaged in Pt@mSiO$_2$ nanoparticles are mostly composed of cubic and cuboctahedral shapes, exposing mostly (100) and (111) surfaces, which explains why the ignition temperature of the Pt@mSiO$_2$ nanoparticles is between those of Pt(100) and Pt(111) single crystals. The Pt@mSiO$_2$ nanoparticles exhibited lower activation energies (27.5 and 9.8 kcal mol^{-1} for below and above the ignition temperature, respectively) than Pt(111) single crystal (42 and 14 kcal mol^{-1}) [86] and (100) single crystal (32.9 kcal mol^{-1} for below ignition) [81]. For catalytic reactions on the surface to occur, the reacting molecules, reaction intermediates and products must alter their bond distances to enable rapid rearrangement. A relatively small number of bonds must also be broken and reformed as the catalytic chemistry occurs. The chemical bonds rearrange more easily on nanoparticles, where fewer atoms participate in the restructuring during catalytic turnover, than on single-crystal surfaces, and this phenomenon might be responsible for the origin of the lower activation energies.

4. Summary and future perspectives

This chapter reviewed synthesis, characterization, and catalytic reaction studies of 3D model catalytic systems based on two distinct materials: colloidal metal nanoparticles and mesoporous silica supports. Pt and Rh nanoparticles with controlled particle size (1 – 15 nm)

and/or shape (cube, cuboctahedron, octahedron, and porous) were synthesized. The nanoparticles were incorporated into the pores of mesoporous silica compounds by capillary inclusion and nanoparticle encapsulation methods. The prepared high surface area 3D model nanocatalysts were characterized by physicochemical methods including XRD, SAXS, TEM, nitrogen physisorption, chemisorptions, and IR of adsorbed CO. The results revealed that the nanoparticles were homogeneously dispersed within the pores of mesoporous silicas while preserving the periodic porous structures of mesoporous supports, and the surface-capping PVP polymers could be effectively removed by careful thermal treatments. The Pt and Rh particles supported mesoporous silica exhibited size- and shape-dependent catalytic activity and selectivity in a variety of model catalytic reactions. The activities of ethane hydrogenolysis by Pt and CO oxidation by Rh were dependent on the metal particle size. In multipath reactions including cyclohexene hydrogenation/dehydrogenation, crotonaldehyde hydrogenation, and pyrrole hydrogenation, the catalytic selectivity changed as a function of Pt particle size.

In the model catalytic studies presented herein, it is particularly significant that three aspects of catalysis, synthesis, characterization, and reaction studies were investigated together in the same laboratory. The integrated approach to catalysis research would provide a new impetus in the catalysis research that increasingly requires energy-efficient and environmentally-benign processes in a “green chemistry” era. The capability of colloidal synthesis have led to the precise control of size and shape of catalytic nanoparticles, whereas the developments of novel *in situ* characterization techniques such as high pressure X-ray photoelectron spectroscopy have enabled the monitoring of dynamic behavior of nanoparticles under reaction conditions. The information gained from reaction studies can be directly utilized to the design and characterizations of new catalysts in an iterative manner, which would ultimately produce a catalyst exhibiting near 100%

selectivity at maximum activity and long-term thermal and chemical stability.

One example of this approach to new catalyst design exemplified in this review is the preparation of thermally stable core-shell structured Pt@mSiO_2 nanocatalyst. Although colloidal nanoparticles have continuously showed promise as model nanocatalysts, the nanoparticles stabilized by organic capping agents are subject to the deformation, melting, and aggregation under high-temperature and/or harsh reaction conditions, which in turn limited their extensive applications. The lessons from such reaction studies triggered a development of nanoparticle catalysts stabilized by porous inorganic shells instead of organic capping agents. The Pt@mSiO_2 nanocatalyst thus prepared showed catalytic activity as high as bare Pt nanoparticles in CO oxidation, and the morphology of pristine particle was preserved up to 1023 K.

By practicing catalytic research in this way, the advances in model catalytic studies can be significantly accelerated, and this would in turn lead to the rapid transfer of results obtained from model catalysts to catalysts used in commercial chemical processes.

Acknowledgements

The work presented in this review was supported by the Director, Office of Science, Office of Basic Energy Sciences, Division of Materials Sciences and Engineering of the US Department of Energy under Contract No. DE-AC02-05CH11231.

References

[1] G. A. Somorjai, J. Y. Park, *Angew. Chem. Int. Ed.* 47 (2008) 9212.

[2] J. M. Thomas, R. Raja, D. W. Lewis, *Angew. Chem. Int. Ed.* 44 (2005) 6456.

[3] G. A. Somorjai, *Introduction to Surface Chemistry and Catalysis*, Wiley, New York, 1994.

[4] G. Ertl, *Angew. Chem. Int. Ed*. 15 (1976) 391.

[5] G. A. Somorjai, A. M. Contreras, M. Montano, R. M. Rioux, *Proc. Natl. Acad. Sci. USA* 103 (2006) 10577.

[6] G. A. Somorjai, J. Y. Park, *J. Chem. Phys.* 128 (2008) 182504.

[7] A. R. Tao, S. Habas, P. Yang, *Small* 4 (2008) 310.

[8] Y. Xia, Y. Xiong, B. Lim, S. E. Skrabalak, *Angew. Chem. Int. Ed*. 48 (2009) 60.

[9] T. S. Ahmadi, Z. L. Wang, T. C. Green, A. Henglein, M. A. El-Sayed, *Science* 272 (1996) 1924.

[10] T. Teranish, M. Hosoe, T. Tanaka, M. Miyake, *J. Phys. Chem. B* 103 (1999) 3818.

[11] Y. Wang, J. Ren, K. Deng, L. Gui, Y. Tang, *Chem. Mater.* 12 (2000) 1622.

[12] Y. Zhang, M. E. Grass, S. E. Habas, F. Tao, T. Zhang, P. Yang, G. A. Somorjai, *J. Phys. Chem. C* 111 (2007) 12243.

[13] M. Boudart, *Adv. Catal. Rel. Subj*. 20 (1969) 153.

[14] P. Gallezot, *Catal. Rev. Sci. Eng.* 20 (1979) 21.

[15] M. Boudart, M. G. Samant, R. Ryoo, *Ultramicroscopy* 20 (1986) 125.

[16] R. M. Crooks, M. Q. Zhao, L. Sun, V. Chechik, L. K. Yeung, *Acc. Chem. Res.* 34 (2001) 181.

[17] R.W. J. Scott, O. M. Wilson, R. M. Crooks, *J. Phys. Chem. B* 109 (2005) 692.

[18] H. Lang, R. A. May, B. L. Iversen, B. D. Chandler. *J. Phys. Chem. B* 125 (2003) 14832.

[19] W. Huang, J. N. Kuhn, C. K. Tsung, Y. Zhang, S. E. Habas, P. Yang, G. A. Somorjai, *Nano Lett.*8 (2008) 2027.

[20] B. Wiley, Y. G. Sun, Y. N. Xia, *Langmuir* 21 (2005) 8077.

[21] F. Kim, S. Connor, H. Song, T. Kuykendall, P. Yang, *Angew. Chem. Int. Ed.* 43 (2004) 3673.

[22] H. Song, F. Kim, S. Connor, G. A. Somorjai, P. Yang, *J. Phys. Chem. B* 109 (2005) 188.

[23] R. M. Rioux, H. Song, M. Grass, S. Habas, K. Niesz, J. D. Hoefelmeyer, P. Yang, G. A.

Somorjai, *Topics in Catal.* 39 (2006) 167.

[24] M. E. Grass, Y. Yue, S. E. Habas, R. M. Rioux, C. I. Teall, P. Yang, G. A. Somorjai, *J. Phys. Chem. B* 112 (2008) 4797.

[25] H. Lee, S. E. Habas, S. Kweskin, D. Butcher, G. A. Somorjai, P. Yang, *Angew. Chem. Int. Ed.* 45 (2006) 7824.

[26] C.-K. Tsung, J. N. Kuhn, W. Huang, C. Aliaga, L.-I. Hung, G. A. Somorjai, P. Yang, *J. Am. Chem. Soc.* submitted.

[27] Y. Zhang, M. E. Grass, J. N. Kuhn, F. Tao, S. E. Habas, W. Huang, P. Yang, G. A. Somorjai, *J. Am. Chem. Soc.* 130 (2008) 5868.

[28] M. E. Davis, *Nature* 417 (2002) 813.

[29] C. T. Kresge, M. E. Leonowicz, W. J. Roth, J. C. Vartuli, J. S. Beck, *Nature* 359 (1992) 710.

[30] Q. Huo, D. I. Margolese, U. Ciesla, P. Feng, T. E. Gier, P. Sieger, R. Leon, P. M. Petroff, F. Schüth, G. D. Stucky, *Nature* 368 (1994) 317.

[31] J. Y. Ying, C. P. Mehnert, M. S. Wong, *Angew. Chem. Int. Ed.* 38 (1999) 56.

[32] D. Trong On, D. Desplantier-Giscard, C. Danumah, S. Kaliaguine, *Appl. Catal. A* 253 (2003) 545.

[33] A. Taguchi, F. Schüth, *Microporous Mesoporous Mater.* 77 (2005) 1.

[34] D. Zhao, Q. Huo, J. Feng, B. F. Chmelka, G. D. Stucky, *J. Am. Chem. Soc.* 120 (1998) 6024.

[35] P. Schmidt-Winkel, W. W. Lukens, Jr., P. Yang, D. I. Margolese, J. S. Lettow, J. Y. Ying, G. D. Stucky, *Chem. Mater.* 12 (2000) 686.

[36] R. M. Rioux, H. Song, J. D. Hoefelmeyer, P. Yang, G. A. Somorjai, *J. Phys. Chem. B* 109 (2005) 2192.

[37] H. Song, R. M. Rioux, J. D. Hoefelmeyer, R. Komor, K. Niesz, M. Grass, P. Yang, G. A. Somorjai, *J. Am. Chem. Soc.* 128 (2006) 3027.

[38] J. E. Benson, M. Boudart, *J. Catal.* 4 (1965) 704.

[39] U. K. Singh, M. A. Vannice, *J. Catal.* 191 (2000) 165.

[40] J. R. Anderson, *Structure of Metallic Catalysts*, Academic Press, New York (1975).

[41] S. S. Kim, A. Karkamkar, T. J. Pinnavaia, M. Kruk, M. Jaroniec, *J. Phys. Chem. B* 105 (2001) 7663.

[42] R. van Hardeveld, F. Hartog, *Surf. Sci.* 15 (1969) 189.

[43] M. E. Grass, S. H. Joo, Y. Zhang, G. A. Somorjai, manuscript in preparation.

[44] R. Narayanan, M. A. El-Sayed, *J. Phys. Chem. B* 109 (2005) 12663.

[45] F. Zaera, F. *Catal. Today* 81 (2003) 149.

[46] G. W. Huber, A. Corma, *Angew. Chem. Int. Ed.* 46 (2007) 7184.

[47] D. Ciuparu, M. R. Lyubovsky, E. Altman, L. D. Pfefferle, A. Datye, A. *Catal. Rev.* 44 (2002) 593.

[48] S. H. Joo, J. Y. Park, C.-K. Tsung, Y. Yamada, P. Yang, G. A. Somorjai, *Nature Mater.* 8 (2009) 126.

[49] F. Zaera, G. A. Somorjai, *J. Am. Chem. Soc.* 106 (1984) 2288.

[50] J. C. Schlatter, M. Boudart, *J. Catal.* 24 (1972) 482.

[51] R. D. Cortright, S. A. Goddard, J. E. Rekoske, J. A. Dumesic, *J. Catal.* 127 (1991) 342.

[52] G. A. Martin, *J. Catal.* 60 (1979) 452.

[53] J. L. Carter, J. A. Cusumano, J. H. Sinfelt, *J. Phys. Chem.* 70 (1966) 2257.

[54] J. H. Sinfelt, W. F. Taylor, D. J. C. Yates, *J. Phys. Chem.* 69 (1965) 95.

[55] J. G. Goodwin, S. Kim, W. D. Rhodes, in J. J. Spivey (ed.) Catalysis, The Royal Society of Chemistry: Cambridge, U.K., 2004; Vol. 17, Chapter 8.

[56] D. W. Goodman, *Surf. Sci.* 123 (1980) L679.

[57] R. D. Cortright, R. M. Watwe, B. E. Spiewak, J. A. Dumesic. *Catal. Today* 53 (1999) 395.

[58] B. S. Gudkov, L. Guczi, P. Tétényi, *J. Catal.* 74 (1982) 207.

[59] R. M. Watwe, B. E. Spiewak, R. D. Cortright, J. A. Dumesic, *J. Catal.* 180 (1998) 184.

[60] R. M. Watwe, R. D. Cortright, J. K. Nørskov, J. A. Dumesic, *J. Phys. Chem. B* 104 (2000) 2299.

[61] R. M. Rioux, B. B. Hsu, M. E. Grass, H. Song, G. A. Somorjai, *Catal. Lett.* 126 (2008) 10.

[62] Z. Paál, *J. Catal.* 91 (1985) 181.

[63] K. R. McCrea, G. A. Somorjai, *J. Mol. Catal. A* 163 (2000) 43.

[64] M. Yang, R. M. Rioux, G. A. Somorjai, *J. Catal.* 237 (2006) 255.

[65] K. M. Bratlie, L. D. Flores, G. A. Somorjai, *Surf. Sci.* 599 (2005) 93.

[66] E. Segal, R. J. Madon, M. Boudart, *J. Catal.* 52 (1978) 45.

[67] P. Gallezot, D. Richard, *Catal. Rev. Sci. Eng.* 40 (1998) 81.

[68] M. E. Grass, R. M. Rioux, G. A. Somorjai, *Catal. Lett.* in press.

[69] G. F. Santori, M. L. Casella, G. J. Siri, H. R. Aduriz, O. A. Ferretti, *React. Kinet. Catal. Lett.* 75 (2002) 225.

[70] A. Giroir-Fendler, D. Richard, P. Gallezot, *Catal. Lett.* 5 (1990) 175.

[71] M. Englisch, A. Jentys, J. A. Lercher, *J. Catal.* 166 (1997) 25.

[72] F. Delbecq, P. Sautet, *J. Catal.* 152 (1995) 217.

[73] E. Furimsky, F. E. Massoth, *Catal. Rev.* 47 (2005) 297.

[74] J. N. Kuhn, W. Huang, C.-K. Tsung, Y. Zhang, G. A. Somorjai, *J. Am. Chem. Soc.* 130 (2008) 14026.

[75] A. Bunch, L. Zhang, G. Karakas, U. S. Ozkan, *Appl. Catal. A: Gen.* 190 (2000) 51.

[76] U. S. Ozkan, L. Zhang, P. A. Clark, *J. Catal.* 172 (1997) 294.

[77] M. Boudart, *J. Mol. Catal.* 30 (1985) 27.

[78] G. C. Bond, *Chem. Soc. Rev.* 20 (1991) 441.

[79] I. Langmuir, *Trans. Frad. Soc.* (1922) 621.

[80] C. T. Campbell, G. Ertl, H. Kuipers, J. Segner, *J. Chem. Phys.* 73 (1980) 5862.

[81] P. J. Berlowitz, C. H. F. Peden, D. W. Goodman, *J. Phys. Chem.* 92 (1988) 5213.

[82] M. S. Chen, Y. Cal, Z. Yan, K. K. Gath, S. Axnanda, D. W. Goodman, *Surf. Sci.* 601 (2007) 5326.

[83] M. E. Grass, Y. Zhang, D. R. Butcher, J. Y. Park, Y. Li, H. Bluhm, K. Bratlie, T. Zhang, G. A. Somorjai, *Angew. Chem. Int. Ed.* 47 (2008) 8893.

[84] S. H. Oh, C. C. Eickel, *J. Catal.* 128 (1991) 526.

[85] K. R. McCrea, J. S. Parker, G. A. Somorjai, *J. Phys. Chem. B* 106 (2002) 10854.

[86] X. C. Su, P. S. Cremer, Y. R. Shen, G. A. Somorjai, *J. Am. Chem. Soc.* 119 (1997) 3994.

Table 1. Average particle sizes and ethylene hydrogenation rates for Pt/SBA-15 catalysts prepared by both capillary inclusion (CI) and nanoparticle encapsulation (NE) methods.

		Particle size (nm)		Ethylene hydrogenation		
Catalyst[a]	Dispersion, D[b]	chemisorption[c]	XRD	Activity[d] (μmol g^{-1} s^{-1})	TOF[e] (s^{-1})	E_a[f] (kcal mol^{-1})
3.2% Pt/SiO_2-IE	1			623	3.8	8
CI series catalysts						
0.73% Pt(1.7 nm)/SBA-15	0.31	3.6		8.3	0.71	6.9
0.95% Pt(2.9 nm)/SBA-15	0.25	4.6	3.0	8.5	0.7	7.9
1.0% Pt(3.6 nm)/SBA-15	0.20	5.6	3.8	6.7	0.64	6.9
1.01% Pt(7.1 nm)/SBA-15	0.13	8.7	7.8	4.2	0.62	8.2
NE series catalysts						
0.6% Pt(1.7 nm)/SBA-15	0.41	0.41	2.7	45	3.5	10.5
0.77% Pt(2.9 nm)/SBA-15	0.36	0.36	3.1	50	3.5	9.8
0.6% Pt(3.6 nm)/SBA-15	0.27	0.27	4.2	28	3.4	10.1
0.62% Pt(7.1 nm)/SBA-15	0.11	0.11	9.5	11	3.2	12.1

[a]Pt content determined by inductively-coupled plasma-atomic emission spectrometry (ICP-AES).

[b]Based on total H_2-O_2 titration uptake at $P = 0$.

[c]Based on d(nm) = 1.13/D.

[d]Initial activity. Reaction conditions were 10 Torr C_2H_4, 100 Torr H_2, and 298 K.

[e]Normalized to the number of surface atoms determined by total H_2-O_2 titration.

[f]Reaction conditions for capillary inclusion series, see [36]. Reaction conditions for nanoparticle encapsulation series, see [37]

Table 2. Turnover rates and kinetic parameters of ethane hydrogenolysis on Pt catalysts

Catalyst[a]	Activity[b] (μmol g^{-1} s^{-1})	TOF[b,c] (s^{-1})	E_a[d] (kcal mol^{-1})	reaction orders	
				C_2H_6[e]	H_2[f]
3.2% Pt/SiO_2-IE	10.6	6.5	54.5	9.6	-2.8
0.6% Pt(1.7 nm)/SBA-15	0.16	1.2	63.4	0.97	-2.4
0.77% Pt(2.9 nm)/SBA-15	7.8×10^{-2}	0.6	68.7	1	-3.1
0.6% Pt(3.6 nm)/SBA-15	1.1×10^{-2}	0.1	75.8	1.1	-3.0
0.62% Pt(7.1 nm)/SBA-15	6.5×10^{-3}	0.08	74.5	0.97	-2.9

[a]Actual catalyst loading determined by ICP-AES.

[b]Reaction conditions were 20 Torr C_2H_6, 200 Torr H_2, and 658 K.

[c]Normalized to the number of surface atoms determined by total H_2−O_2 titration.

[d]Reaction conditions were 20 Torr C_2H_6, 200 Torr H_2, and 593−673 K.

[e]Reaction conditions were 10−60 Torr C_2H_6, 200 Torr H_2, and 658 K.

[f]Reaction conditions were 20 Torr C_2H_6, 140−270 Torr H_2, and 658 K.

Table 3. The activity and selectivity for cyclohexene hydrogenation–dehydrogenation and the apparent activation energy of Pt/SBA-15 catalysts

	Particle size by chemisorption[b]	Hydrogenation			Dehydrogenation		
Catalyst[a]	(nm)	Activity[c] (μmol g^{-1} s^{-1})	TOF[d] (s^{-1})	E_a[e] (kcal mol^{-1})	Activity[c] (μmol g^{-1} s^{-1})	TOF[d] (s^{-1})	E_a[f] (kcal mol^{-1})
3.2% Pt/SiO_2-IE	1	590	3.6	9.6	623	3.8	8
0.6% Pt(1.7 nm)/SBA-15	2.7	41	3.2	8.7	45	3.5	10.5
0.77% Pt(2.9 nm)/SBA-15	3.1	56	3.9	9.1	50	3.5	9.8
0.6% Pt(3.6 nm)/SBA-15	4.2	31	3.7	9.4	28	3.4	10.1
0.62% Pt(7.1 nm)/SBA-15	9.4	19	4.9	9.8	11	3.2	12.1
Pt(111)[g]			14.6[h]	8.6			
Pt(100)[g]			1.3[h]	18.8			

[a]Particle size determined by counting >200 particles from TEM micrographs

[b]Determined from the total H_2 uptake after O_2 chemisorption (H_2–O_2 titration) and d(nm) = 1.13/D, where D is the dispersion

[c]Standard conditions are 10 Torr C_6H_{10}, 200 Torr H_2, and 313 K (hydrogenation) or 423 K (dehydrogenation)

[d]Normalized by the total number of surface atoms measured by H_2–O_2 titration

[e]Standard conditions were 10 Torr C_6H_{10}, 200 Torr H_2, and 273–323 K for the supported catalysts. The activity in this temperature regime displays 'normal' Arrhenius temperature-dependent behavior

[f]Standard conditions were 10 Torr C_6H_{10}, 200 Torr H_2, and 398–443 K for the supported catalysts. The activity in this temperature regime displays 'normal' Arrhenius temperature-dependent behavior

[g]From reference [63].

[h]The original reaction conditions were 10 Torr C_6H_{10}, 100 Torr H_2, balance He and temperatures specified in (c). The rates were corrected to standard conditions assuming 0.75 order H_2 dependence for hydrogenation [66] and 0.2 reaction order for dehydrogenation (this work)

Table 4. Dispersion, and activity and selectivity for crotonaldehyde hydrogenation of Pt/SBA-15 catalysts.

	Pt loading[a] (wt %)	Dispersion, D[b]	TOF[c] (s^{-1})	$S_{crotyl\ alcohol}$[d] (%)	E_a[e] (kcal mol^{-1})
Pt(1.7 nm)/SBA-15	0.58	0.33	2.1	13.7	10.8
Pt(2.9 nm)/SBA-15	1.28	0.18	2.9	17.0	11.2
Pt(3.6 nm)/SBA-15	1.61	0.15	4.3	21.6	10.8
Pt(7.1 nm)/SBA-15	2.43	0.08	4.8	33.9	11.7

[a]Loading determined by ICP-OES

[b]Irreversible H_2 chemisorption at 303 K, extrapolated to $P = 0$

[c]Overall crotonaldehyde hydrogenation rate per surface site at 8 Torr C_6H_4O, 160 Torr H_2 and 353 K

[d]Determined at 8 Torr crotonaldehyde, and 160 Torr H_2 and 353 K

[e]Overall apparent activation energy determined at 8 Torr crotonaldehyde, 160 Torr H_2, and 353–393 K

Scheme Captions

Scheme 1. Reaction pathway of crotonaldehyde hydrogenation.

Scheme 2. Reaction pathway of pyrrole hydrogenation.

Scheme 1.

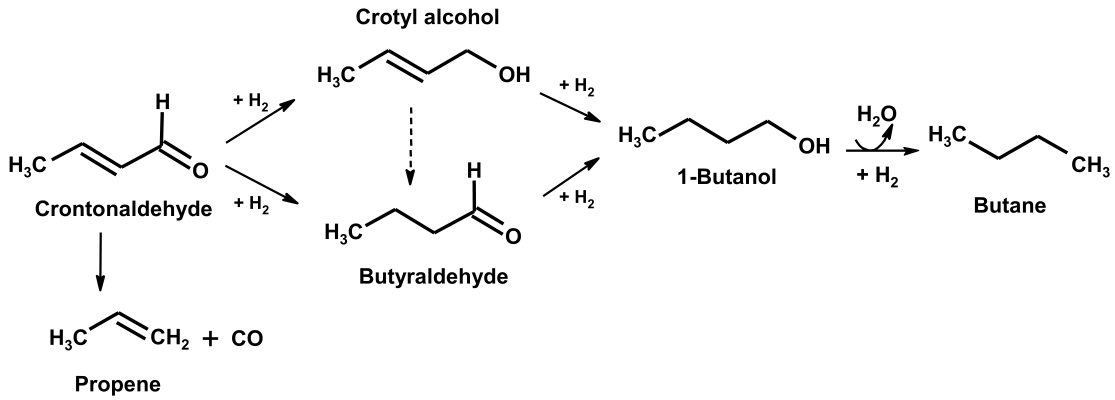
Crotyl alcohol
H3C
OH
+ H2
H
+ H2
H3C
O
Crontonaldehyde
+ H2
H
H3C
O
Butyraldehyde
+ H2
H3C
OH
1-Butanol
H2O
+ H2
H3C
CH3
Butane
H3C
CH2 + CO
Propene

Scheme 2.

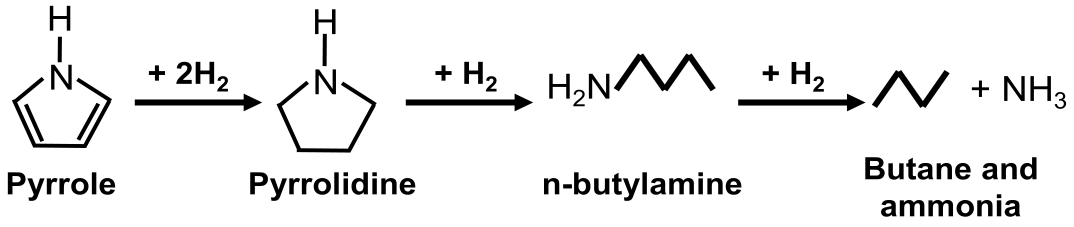
H
N
+ 2H2
H
N
+ H2
H2N
+ H2
+ NH3
Pyrrole
Pyrrolidine
n-butylamine
Butane and ammonia

Figure Captions

Figure 1. Evolution of model catalysts for the studies of heterogeneous catalysis: from single crystals to lithography-based metal nanostructures, and to collidal nanoparticle-based 2D and 3D nanoparticle arrays.

Figure 2. Preparation scheme of high surface area 3D model catalysts by integration of colloidal metal nanoparticles and mesoporous oxide supports. The 3D model catalysts are generated by capillary inclusion and nanoparticle encapsulation methods.

Figure 3. TEM images of Pt nanoparticles of (a) 1.7 nm, (b) 2.9 nm, (c) 3.6 nm, and (d) 7.1 nm. The scale bar is 10 nm. Adapted and modified from ref. [36].

Figure 4. Schematic presentation of dendrimer-templated synthesis of metal nanoparticles and representative TEM image of ~ 1 nm Rh nanoparticles composed of 30 Pt atoms. Adapted and modified from ref. [19].

Figure 5. TEM and HRTEM (insets) images of (a) cuboatahedra, (b) cubes, and (c) porous Pt nanoparticles. The scale bars for TEM and HRTEM images are 50 nm and 3 nm, respectively. Adapted and modified from ref. [25].

Figure 6. Schematic illustration of simultaneous control of size and shape of sub-10 nm Pt nanoparticles. Adapted from ref. [26].

Figure 7. TEM and HRTEM (insets) images of Pt nanoparticles with different shapes and sizes: (a) 9 nm nanocubes, (b) 7 nm nanocubes, (c) 6 nm nanocubes, (d) 5 nm nanocubes, (e) 5 nm nanopolyhedra, and (f) 3.5 nm nuclei. HRTEM images of nanocubes are taken along the [100] zone axis, while a single 5 nm nanopolyhedron and 3.5 nm nucleus are taken along the [111] zone axis The scale bars for TEM and HRTEM images are 20 nm and 1 nm, respectively. Adapted and modified from ref. [26].

Figure 8. The size of Pt nanoparticles as a function of [Pt(IV) to Pt(IV) + Pt(II)] in the initial solution. The blue circles represent nanopolyhedra and the red diamonds represent nanocubes. Adapted from ref. [26].

Figure 9. TEM images of Pt(*X*)/SBA-15 catalysts. *X* = (a) 1.7 nm, (b) 2.9 nm, (c) 3.6 nm, and (d) 7.1 nm. The scale bar is 40 nm. Adapted from ref. [37].

Figure 10. (A) XRD patterns for SBA-15 (a) and Pt(*X*)/SBA-15 catalysts (b-e). *X* = (b) 1.7 nm, (c) 2.9 nm, (d) 3.6 nm, and (e) 7.1 nm. The Pt(111), Pt(110), and Pt(200) peaks of the fcc lattice are indicated for Pt(7.1 nm)/SBA-15. Spectra are offset for clarity. (B) SAXS data for SBA-15 (a) and Pt(*X*)/SBA-15 catalysts (b-e). *X* = (b) 1.7 nm, (c) 2.9 nm, (d) 3.6 nm, and (e) 7.1 nm. The SBA-15(100), (110), and (200) peaks are indicated, demonstrating the long-range order of the channels. Spectra are offset for clarity. Adapted from ref. [37].

Figure 11. Infrared spectrum of CO adsorption at 295 K for the Pt/SBA-15 catalyst series: (a) 2.33% Pt(1.7 nm)/SBA-15, (b) 2.69% Pt(2.9 nm)/SBA- 15, (c) 2.62% Pt(3.6 nm)/SBA-15, and (d) 2.86% Pt(7.1 nm)/SBA-15. (Inset: the peak position and fwhm of the atop CO stretching vibration as a function of particle size at room temperature.) At saturation coverage, the peak position red-shifts due to changes in the average coordination number as the particle decreases. Peak heights have been modified for clarity. Adapted from ref. [37].

Figure 12. TEM images of Rh/SBA-15 catalysts: (a) Rh(1.9 nm)/SBA-15, (b) Rh(2.4 nm)/SBA-15, (c) Rh(6.7 nm)/SBA-15, and (d) Rh(11.3 nm)/SBA-15. Adapted from ref. [43].

Figure 13. Schematic representation of the synthesis of Pt@mSiO_2 nanoparticles. Pt nanoparticles are synthesized using TTAB surfactant as the capping agent, and used as the core particles. Second, as-synthesized Pt@SiO_2 particles are prepared by polymerizing TEOS around the TTAB-capped Pt cores. RT: room temperature. The as-

synthesized Pt@SiO_2 particles are subsequently converted to Pt@mSiO_2 particles by calcination. Adapted and modified from ref. [48].

Figure 14. TEM images of Pt@SiO_2 (a) and Pt@mSiO_2 nanoparticles calcined at 623 K (b), 823 K (c), and 1023 K (d). Adapted and modified from ref. [48].

Figure 15. Dependence of ethane hydrogenolysis turnover frequency and apparent activation energy on Pt particle size. Turnover frequencies were measured at 20 Torr C_2H_6, 200 Torr H_2, and 658 K. Adapted from ref. [37].

Figure 16. The influence of particle size on reaction selectivity during hydrogenation/dehydrogenation of cyclohexene over the series of Pt/SBA-15 catalysts. The reaction conditions were 10 Torr C_6H_{10}, 200 Torr H_2, and 423 K. The inset is the selectivity at 523 K and the same pressure conditions. Adapted from ref. [61].

Figure 17. The effect of particle size on reaction selectivity during crotonaldehyde hydrogenation over the series of Pt/SBA-15 catalysts. The reaction conditions were 8 Torr crotonaldehyde and 160 Torr hydrogen, and 353 K. Adapted from ref. [68].

Figure 18. Pyrrole hydrogenation selectivity (color coordinated to Scheme 2) as a function of Pt NP size at 413 K and 11 ± 2% conversion. Feed was 4 Torr of pyrrole and 400 Torr of H_2 with a He balance. Adapted and modified from ref. [74].

Figure 19. Pyrrole hydrogenation selectivity for Pt nanocrystals with different size and shape as a function of temperature. Solid squares, open squares, and open spheres represent 9 nm nanocubes, 5 nm nanocubes, and 5 nm nanopolyhedra, respectively. Feed was 4 Torr of pyrrole and 400 Torr of H_2 with a He balance. Adapted from ref. [26].

Figure 20. Turnover frequency for CO oxidation as a function of Rh particle size over uncalcined Rh/SBA-15 and calcined-reduced Rh/SBA-15 catalysts. The reaction conditions were 40 Torr CO, 100 Torr O_2, and 443 K. Adapted from ref. [43].

Figure 21. Schematic presentation of the changes in binding mode of CO to Rh nanoparticle surface after different pretreatments. Adapted from ref. [43].

Figure 22. CO oxidation activity of TTAB-capped Pt and Pt@mSiO_2 nanoparticles. Adapted and modified from ref. [48]

Figure 23. Pt nanoparticle morphologies before and after CO oxidation. SEM images of core–shell Pt@mSiO_2 (a,d) and TTAB-capped Pt (b,e) nanoparticle arrays on 2D silicon wafer, and TEM images of TTAB-capped Pt nanoparticles dispersed on a 3D MCF-17 mesoporous silica support (c,f) before (a–c) and after CO oxidation at 603 K (d) and at 573 K (e,f). Adapted from ref. [48].

Figure 1.

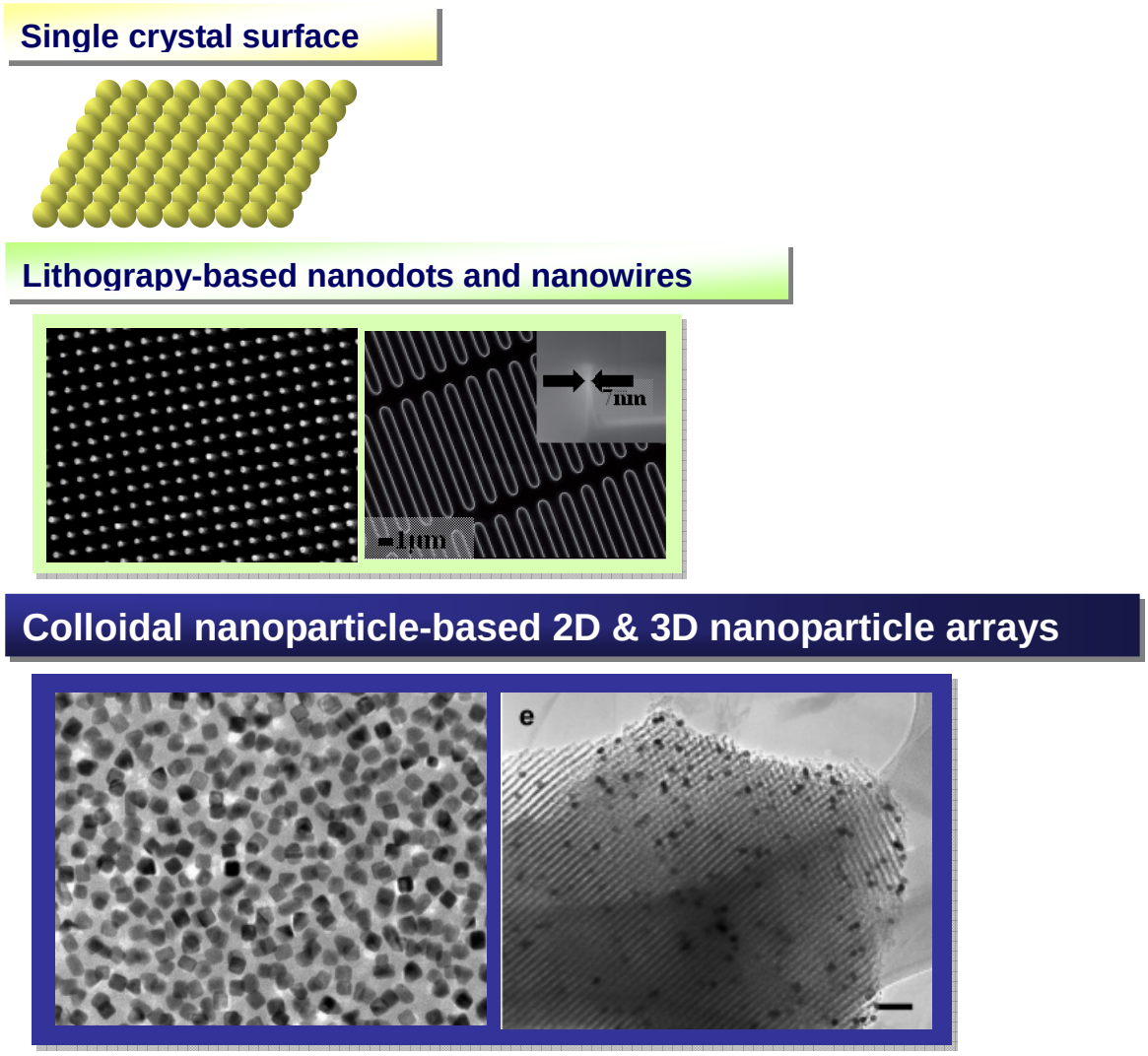
Single crystal surface
Lithograpy-based nanodots and nanowires
1μm
Colloidal nanoparticle-based 2D & 3D nanoparticle arrays
e

Figure 2.

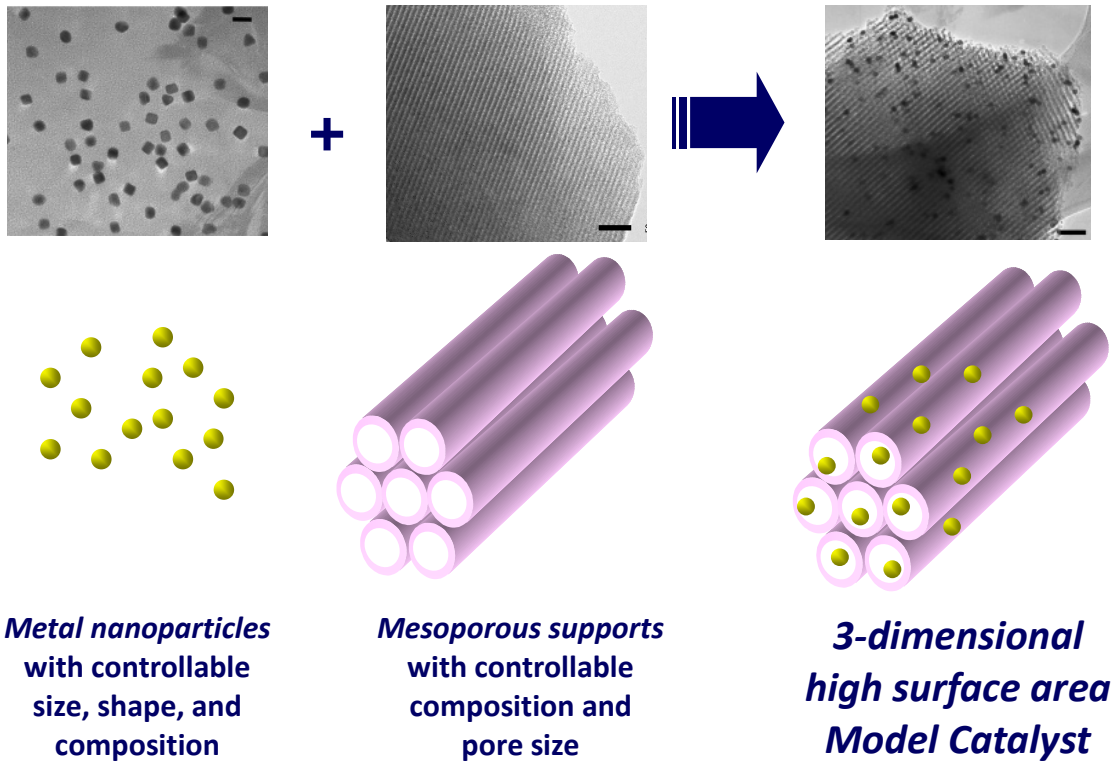
Metal nanoparticles with controllable size, shape, and composition
Mesoporous supports with controllable composition and pore size
3-dimensional high surface area Model Catalyst

Figure 3.

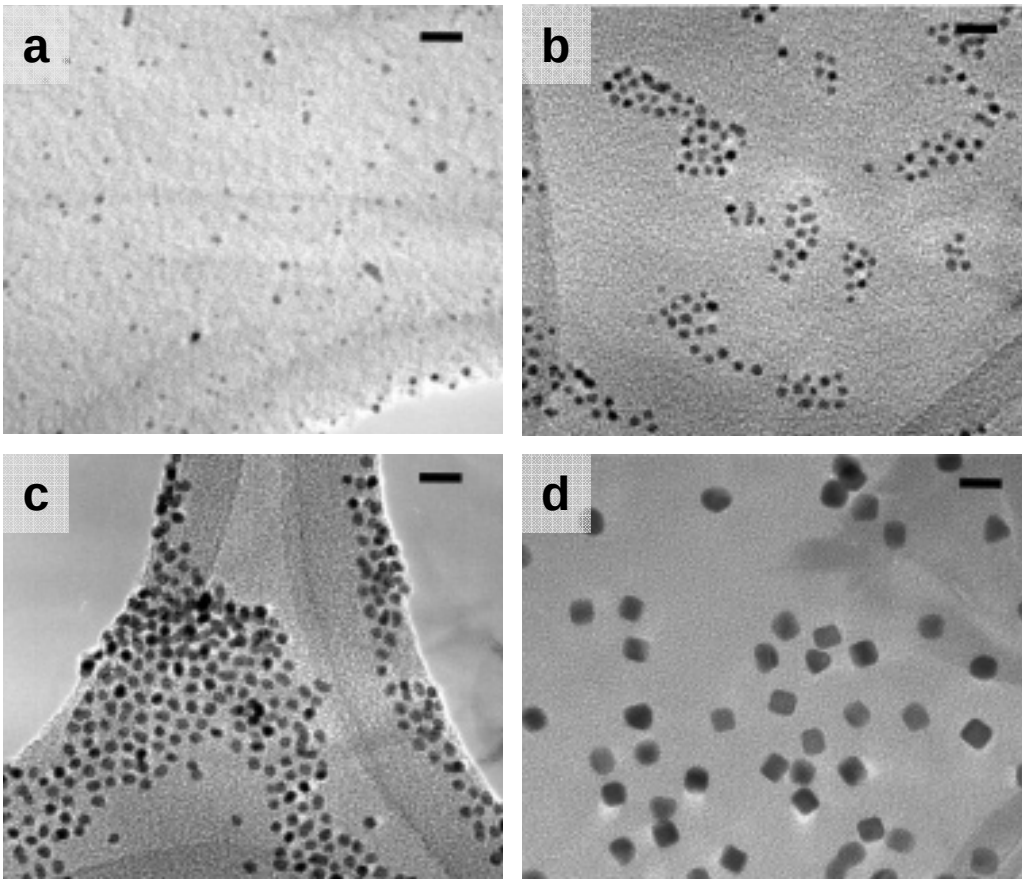

Figure 4.

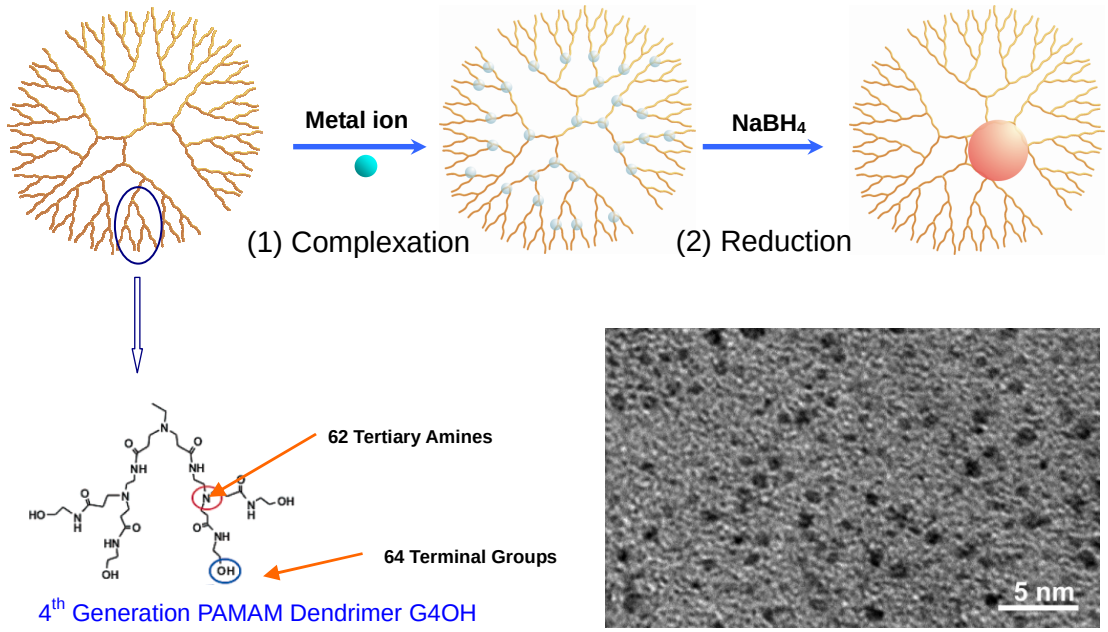
Metal ion
NaBH4
(1) Complexation
(2) Reduction
62 Tertiary Amines
64 Terminal Groups
4th Generation PAMAM Dendrimer G4OH
5 nm

Figure 5.

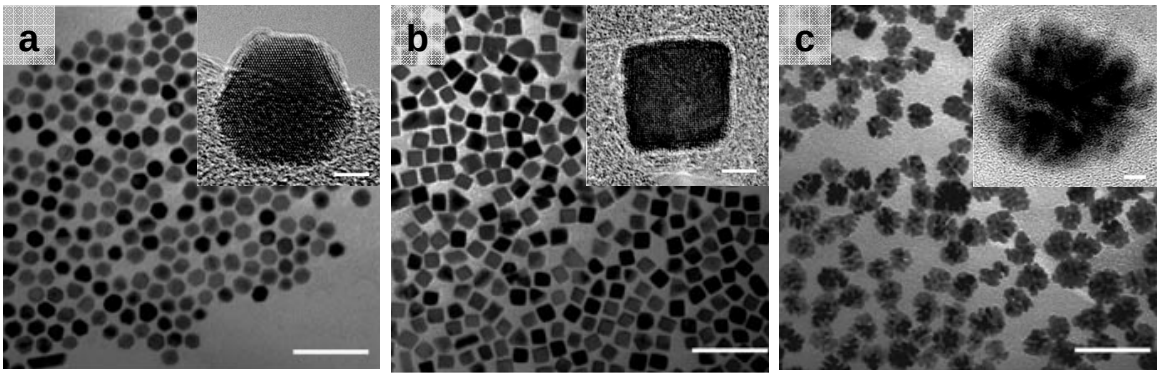

Figure 6.

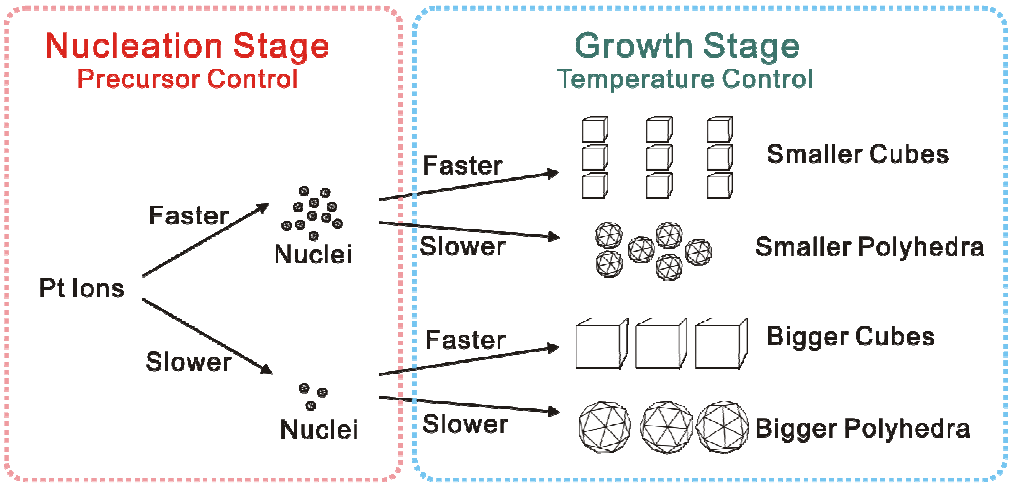
Nucleation Stage
Precursor Control
Growth Stage
Temperature Control
Pt Ions
Faster
Slower
Nuclei
Nuclei
Faster
Slower
Faster
Slower
Smaller Cubes
Smaller Polyhedra
Bigger Cubes
Bigger Polyhedra

Figure 7.

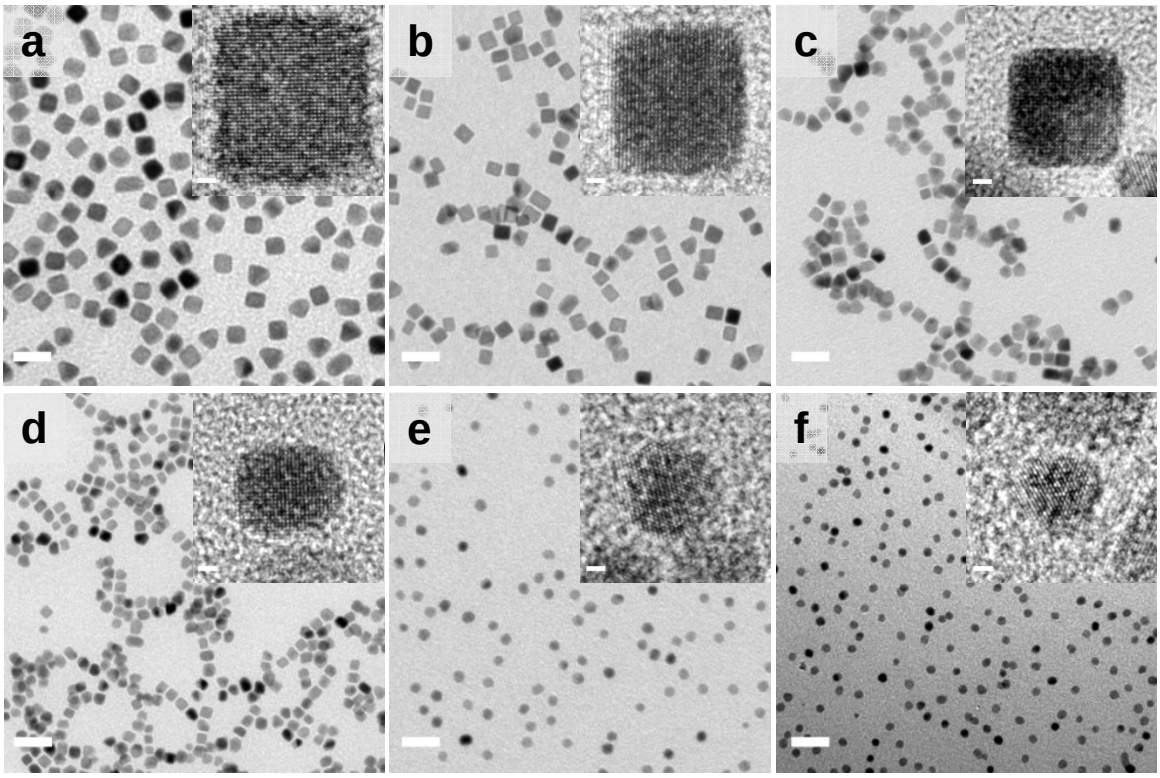

Figure 8.

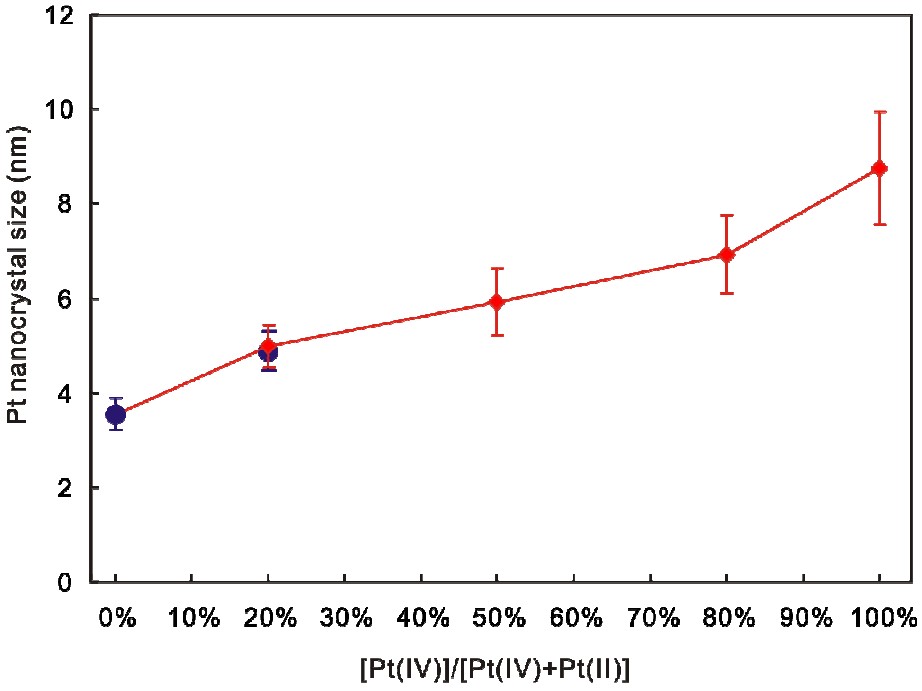
Pt nanocrystal size (nm)
12
10
8
6
4
2
0
0%
10%
20%
30%
40%
50%
60%
70%
80%
90%
100%
[Pt(IV)]/[Pt(IV)+Pt(II)]

Figure 9.

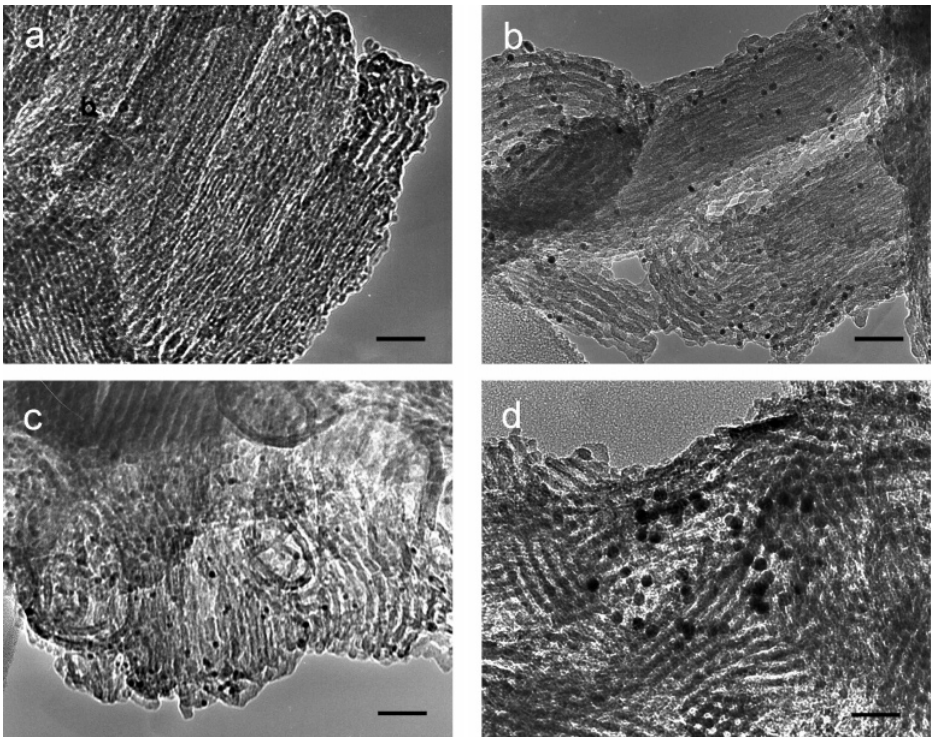

Figure 10.

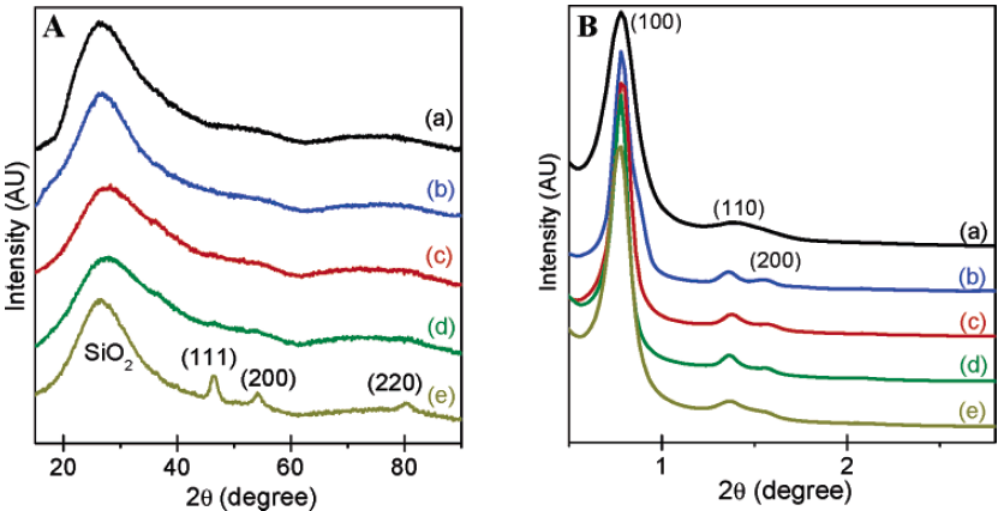
A
Intensity (AU)
(a)
(b)
(c)
(d)
(e)
SiO2
(111)
(200)
(220)
20
40
60
80
2θ (degree)
B
(100)
(110)
(200)
(a)
(b)
(c)
(d)
(e)
1
2
2θ (degree)

Figure 11.

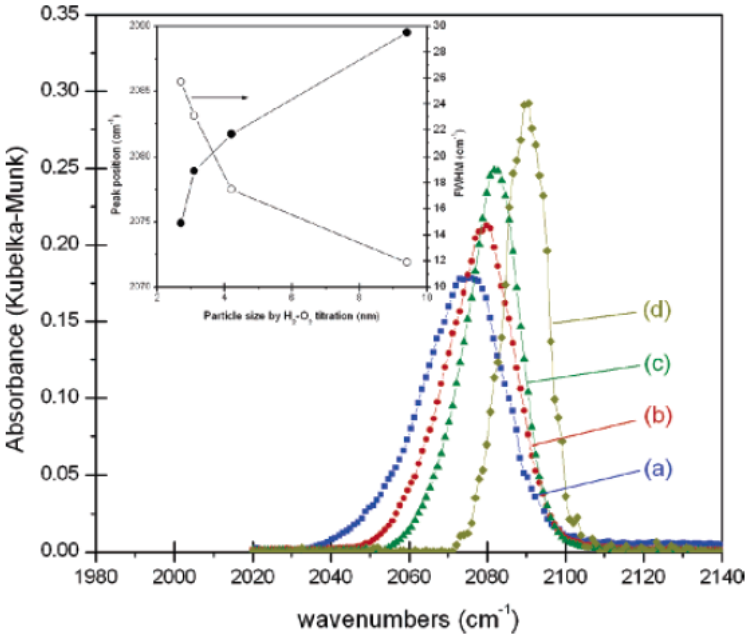
Absorbance (Kubelka-Munk)
wavenumbers (cm-1)
(d)
(c)
(b)
(a)
Peak position (cm-1)
FWHM (cm-1)
Particle size by H2-O2 titration (nm)

Figure 12.

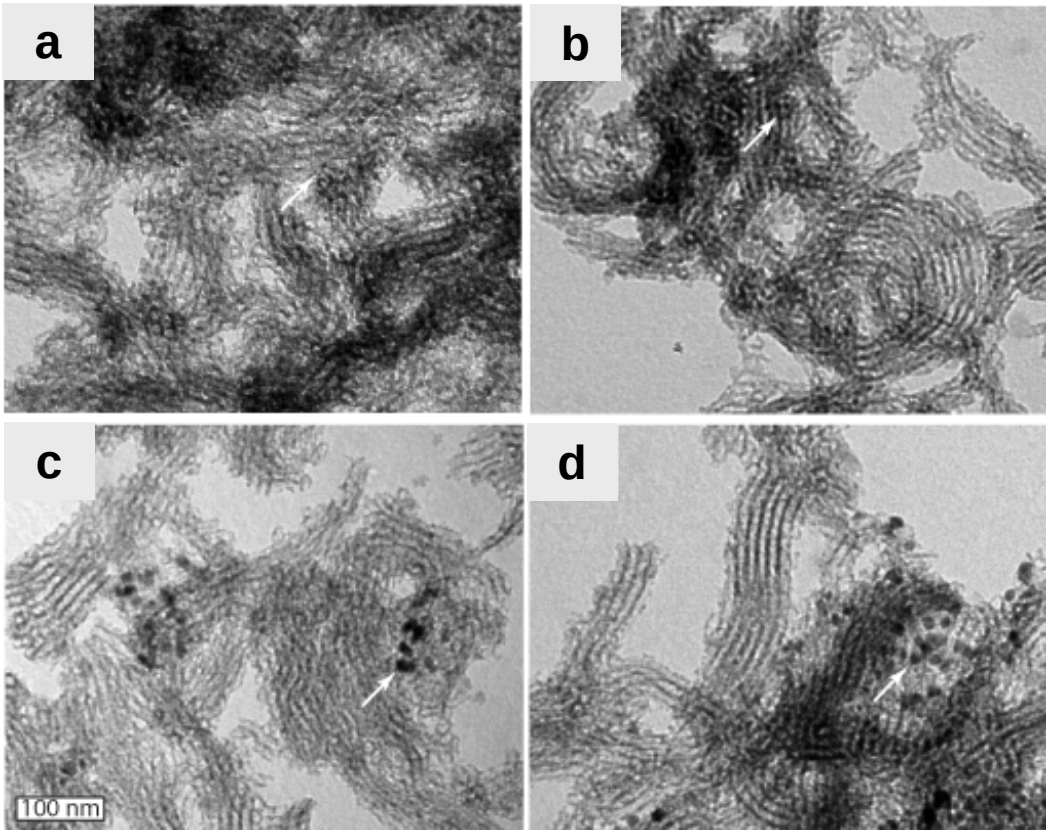

Figure 13.

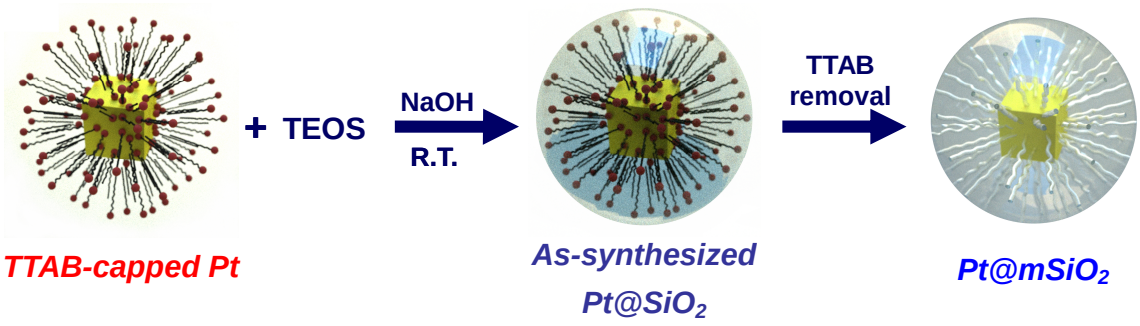
+ TEOS
NaOH
R.T.
TTAB
removal
TTAB-capped Pt
As-synthesized
Pt@SiO2
Pt@mSiO2

Figure 14.

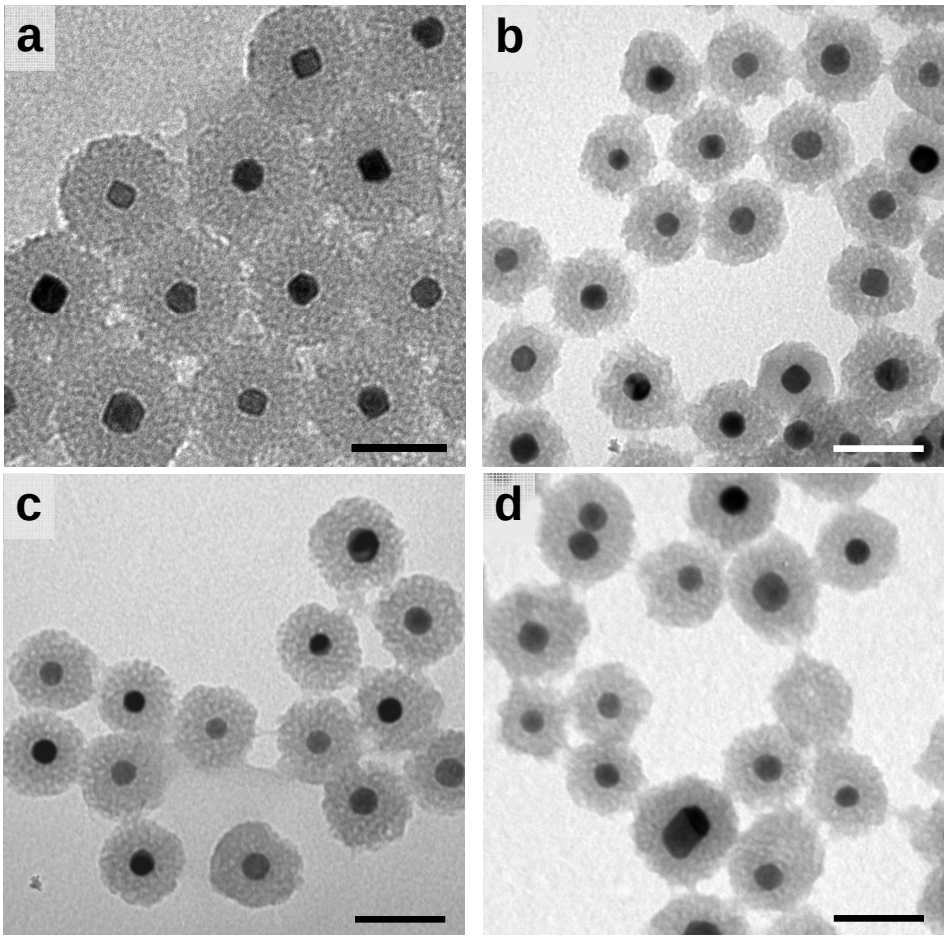

Figure 15.

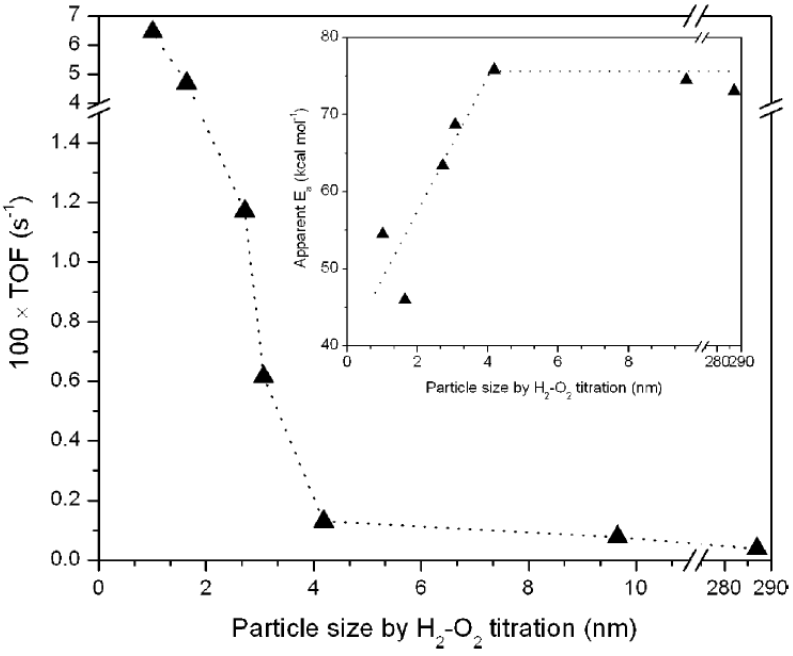
100 × TOF (s^{-1})
Particle size by H_2-O_2 titration (nm)
Apparent E_a (kcal mol^{-1})
Particle size by H_2-O_2 titration (nm)

Figure 16.

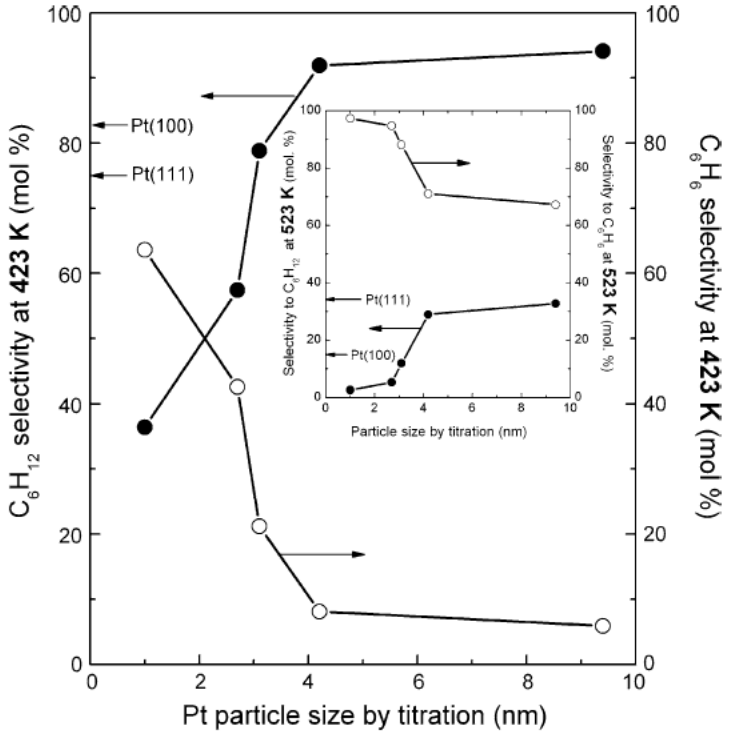
Pt(100)
Pt(111)
C_6H_{12} selectivity at 423 K (mol %)
C_6H_6 selectivity at 423 K (mol %)
Pt particle size by titration (nm)
Selectivity to C_6H_{12} at 523 K (mol. %)
Selectivity to C_6H_6 at 523 K (mol. %)
Particle size by titration (nm)

Figure 17.

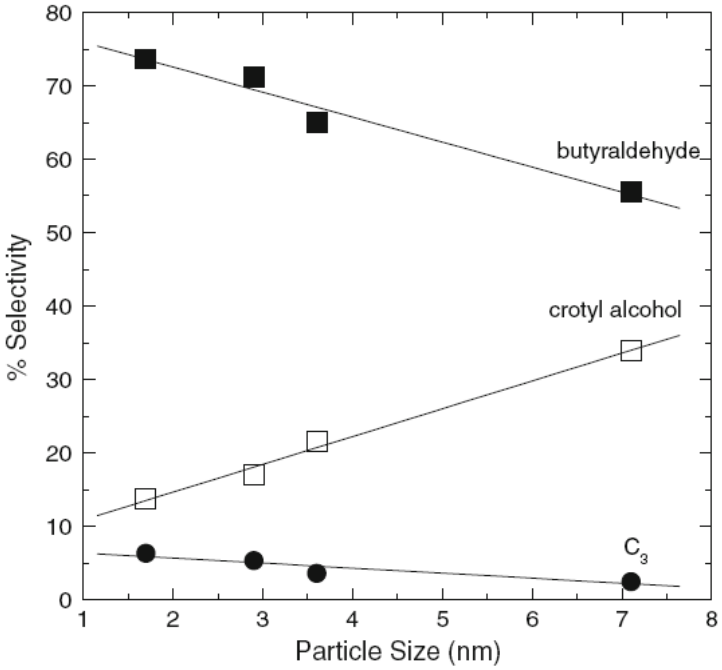
% Selectivity
Particle Size (nm)
butyraldehyde
crotyl alcohol
C_3
0
10
20
30
40
50
60
70
80
1
2
3
4
5
6
7
8

Figure 18.

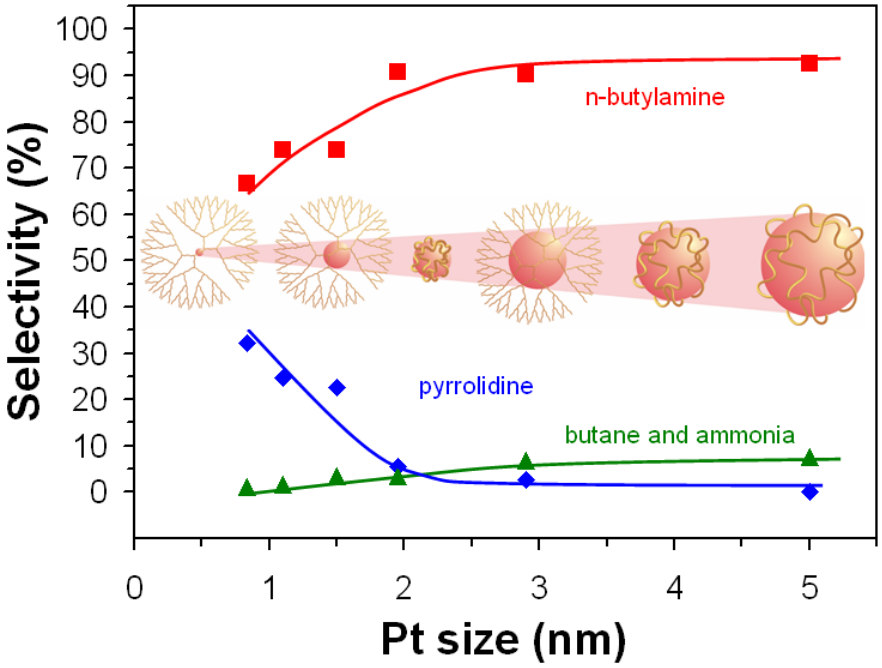
Selectivity (%)
100
90
80
70
60
50
40
30
20
10
0
0
1
2
3
4
5
Pt size (nm)
n-butylamine
pyrrolidine
butane and ammonia

Figure 19.

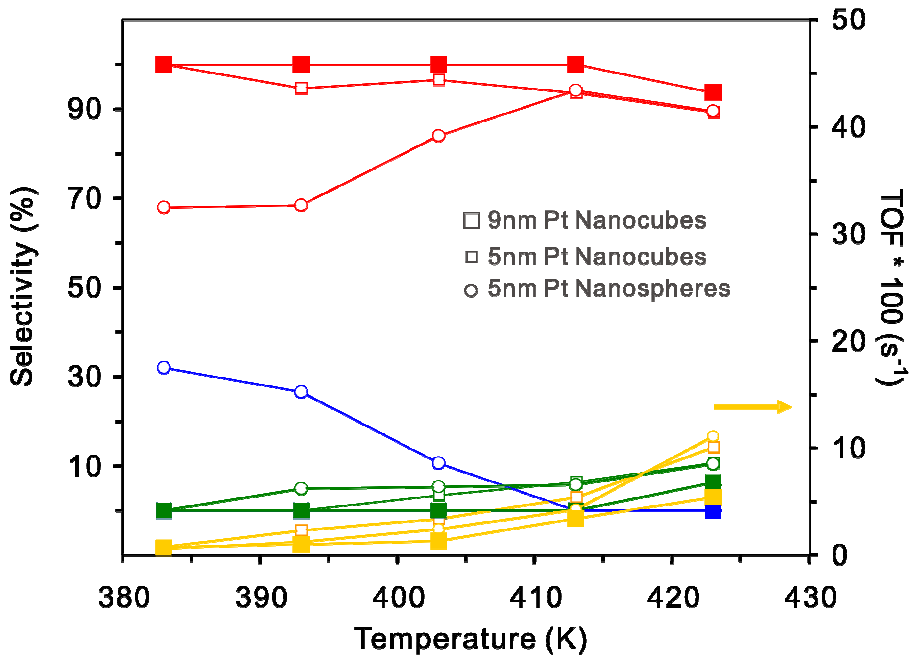
Selectivity (%)
TOF * 100 (s-1)
Temperature (K)
9nm Pt Nanocubes
5nm Pt Nanocubes
5nm Pt Nanospheres
380
390
400
410
420
430
10
30
50
70
90
0
10
20
30
40
50

Figure 20.

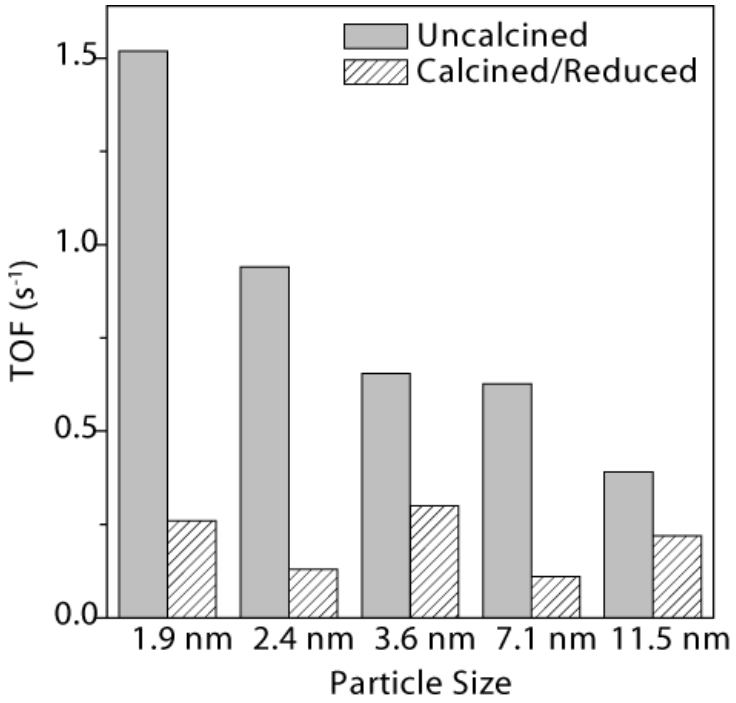
Uncalcined
Calcined/Reduced
1.5
1.0
0.5
0.0
TOF (s-1)
1.9 nm
2.4 nm
3.6 nm
7.1 nm
11.5 nm
Particle Size

Figure 21.

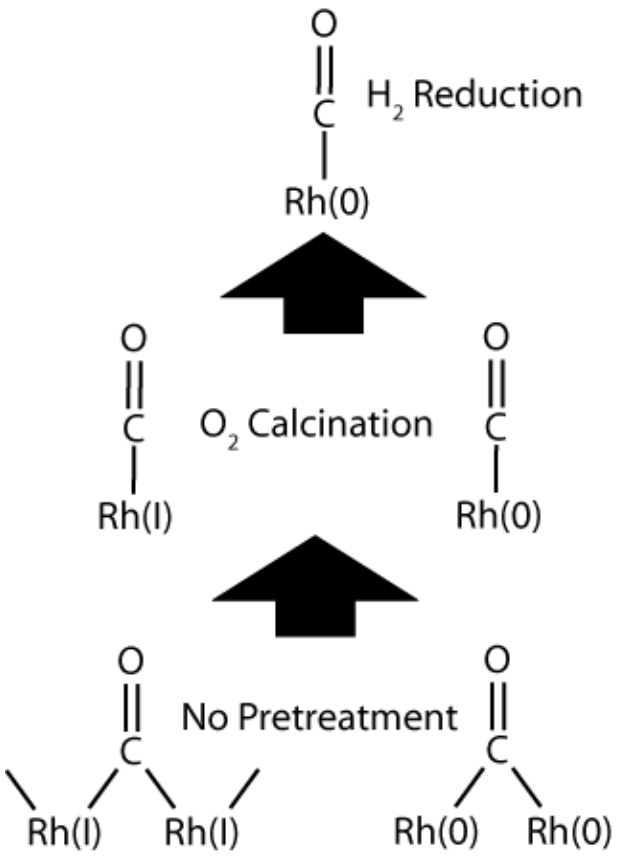
O
C
Rh(0)
H2 Reduction
O
C
Rh(I)
O2 Calcination
O
C
Rh(0)
No Pretreatment
O
C
Rh(I)
Rh(I)
O
C
Rh(0)
Rh(0)

Figure 22.

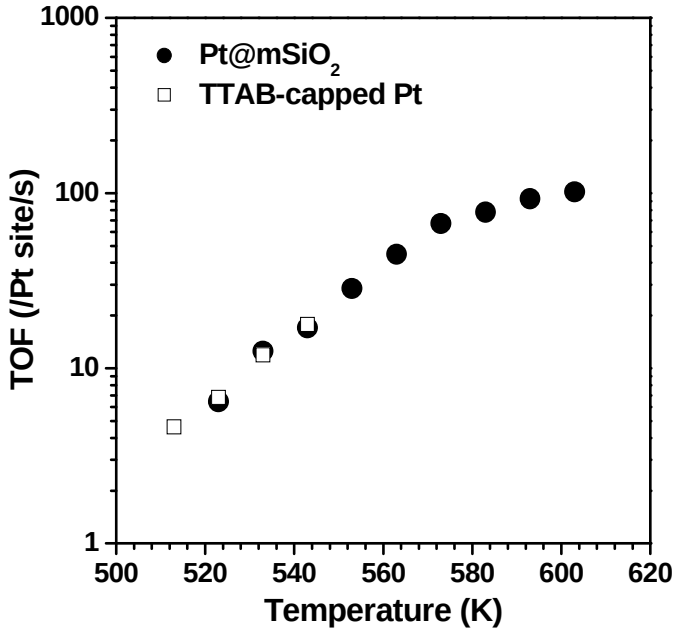
1000
100
10
1
TOF (/Pt site/s)
500
520
540
560
580
600
620
Temperature (K)
Pt@mSiO2
TTAB-capped Pt

Figure 23.